European Journal of Medicinal Chemistry 218 (2021) 113404

Contents lists available at ScienceDirect

European Journal of Medicinal Chemistry

journal homepage: http://www.elsevier.com/locate/ejmech

Square planar Au(III), Pt(II) and Cu(II) complexes with quinoline-substituted 2,2′:6′,2″-terpyridine ligands: From *in vitro* to *in vivo* biological properties

Katarzyna Choroba [a, *], Barbara Machura [a], Agata Szlapa-Kula [a], Jan G. Malecki [a], Luis Raposo [b], Catarina Roma-Rodrigues [b], Sandra Cordeiro [b], Pedro V. Baptista [b], Alexandra R. Fernandes [b, **]

[a] Institute of Chemistry, University of Silesia, Szkolna 9, 40-006, Katowice, Poland
[b] UCIBIO, Departamento de Ciências da Vida, NOVA School of Science and Technology, Campus de Caparica, 2829-516, Caparica, Portugal

ARTICLE INFO

Article history:
Received 7 January 2021
Received in revised form
8 March 2021
Accepted 19 March 2021
Available online 26 March 2021

Keywords:
Square planar metal complexes
Apoptosis
Autophagy induction
Mitochondrial membrane potential changes
Intracellular reactive oxygen species
Ex-ovo chorioallantoic membrane *in vivo* assay

ABSTRACT

Cancer is the second leading cause of death worldwide. Cisplatin has challenged cancer treatment; however, resistance and side effects hamper its use. New agents displaying improved activity and more reduced side effects relative to cisplatin are needed. In this work we present the synthesis, characterization and biological activities of three complexes with quinoline-substituted 2,2′:6′,2″-terpyridine ligand: [Pt(4′-(2-quin)-terpy)Cl](SO_3CF_3) (**1**), [Au(4′-(2-quin)-terpy)Cl](PF_6)$_2$·CH_3CN (**2**) and [Cu(4′-(2-quin)-terpy)Cl](PF_6) (**3**). The three complexes displayed a high antiproliferative activity in ovarian carcinoma cell line (A2780) and even more noticeable in a colorectal carcinoma cell line (HCT116) following the order **3** > **2** > **1**. The complexes IC_{50} are at least 20 × lower than the IC_{50} displayed by cisplatin (15.4 μM) in HCT116 cell line while displaying at the same time, much reduced cytotoxicity in a normal dermal fibroblast culture. These cytotoxic activities seem to be correlated with the inclination angles of *2-quin* unit to the central pyridine. Interestingly, all complexes can interact with calf-thymus DNA (CT-DNA) *in vitro* via different mechanisms, although intercalation seems to be the preferred mechanism at least for **2** and **3** at higher concentrations of DNA. Moreover, circular dichroism (CD) data seems to indicate that complex **3**, more planar, induces a high destabilization of the DNA double helix (shift from B-form to Z-form). Higher the deviation from planar, the lower the cytotoxicity displayed by the complexes. Cellular uptake may be also responsible for the different cytotoxicity exhibited by complexes with **3** > **2** >**1**. Complex **2** seems to enter cells more passively while complex **1** and **3** might enter cells via energy-dependent and -independent mechanisms. Complexes **1**–**3** were shown to induce ROS are associated with the increased apoptosis and autophagy. Moreover, all complexes dissipate the mitochondrial membrane potential leading to an increased BAX/BCL-2 ratio that triggered apoptosis. Complexes **2** and **3** were also shown to exhibit an anti-angiogenic effect by significantly reduce the number of newly formed blood vessel in a CAM model with no toxicity in this *in vivo* model.

Our results seem to suggest that the increased cytotoxicity of complex **3** in HCT116 cells and its potential interest for further translation to pre-clinical mice xenografts might be associated with: 1) higher % of internalization of HCT116 cells via energy-dependent and -independent mechanisms; 2) ability to intercalate DNA and due to its planarity induced higher destabilization of DNA; 3) induce intracellular ROS that trigger apoptosis and autophagy; 4) low toxicity in an *in vivo* model of CAM; 5) potential anti-angiogenic effect.

1. Introduction

Since the discovery of the anticancer properties of *cis*-[$PtCl_2(NH_3)_2$] and its approval for human use as anticancer agent,

* Corresponding author.
** Corresponding author.
E-mail addresses: katarzyna.choroba@us.edu.pl (K. Choroba), ma.fernandes@fct.unl.pt (A.R. Fernandes).

https://doi.org/10.1016/j.ejmech.2021.113404

medicinal inorganic chemistry has become one of the most important research area [1–4]. It is believed that the use of metal-drugs in therapy provides opportunities which are not accessible to pure organic molecules. Despite the spectacular success of cisplatin and its analogues carboplatin and oxaliplatin, widely applied in vast majority of cancer treatments, the design of new biologically active metal–organic coordination compounds remains a great challenge. Much more work is required to obtain agents displaying improved activity profile and more reduced side effects relative to cisplatin chemotherapy.

Scientific attention is currently being paid not only to platinum-based anticancer agents but also to non-platinum anticancer agents, particularly those with bio-essential metal ions [3–5]. Several complexes of titanium(IV), ruthenium(III) or gallium(III), for example $(\eta^5\text{-}C_5H_5)_2TiCl_2$, [InH][*trans*-$RuCl_4In_2$] (KP1019, In – indazole) and $Ga(quin)_3$ (KP46, quin – 8-quinolinol) have entered clinical trials, while iron(III), cobalt(III), copper(II) and gold(III) complexes have been proven to show promising antiproliferative properties [3–7]. Also, different mechanisms of anticancer agent actions have been revealed. A biologically active molecule can interact with DNA strand in covalent (via alkylation or inter- and intrastrand crosslinking, like cisplatin and its analogues) and non-covalent mode – by groove binding (facilitated by van der Waals interactions and hydrogen bonding), intercalation (stabilized by π-π stacking interactions between the drug and DNA bases) or external binding (electrostatic outside-edge stacking interactions) [8–14]. On the other hand, complexes containing redox-active metals may undergo both interaction with DNA and redox reactions, which allow them to interact with other biological molecules [15]. The choice of the metal center determines the redox activity of the drug, while the ligand is responsible for DNA recognition [16]. Most importantly, the compounds showing different type of DNA binding and mechanisms of action than *cis*-$[PtCl_2(NH_3)_2]$ may induce cell death in cisplatin-resistant tumors.

In order to get further insights into the role of metal center and ligand substitution in square-planar coordination compounds, we have synthetized and investigated the molecular structures and antiproliferative properties of three new complexes (Scheme 1) with 2,2′:6′,2″-terpyridine (*terpy*) ligand functionalized with 2-quinolinyl (*2-quin*).

With reference to the previous results concerning biologically active transition metal complexes bearing *terpy*-based ligands [3,5,13,17–28], searching new efficient anticancer agents in this group seems to be particularly justifiable. Chelating ability of *terpy* ligands enhances the complex stability, while their planarity promotes intercalative interaction of the complex with DNA due to π-stacking between the plane of the aromatic rings and DNA base pairs.

2. Results and discussion

2.1. Synthesis and characterization

The preparation of [Pt(4′-(2-quin)-terpy)Cl](SO_3CF_3) (**1**), [Au(4′-(2-quin)-terpy)Cl]$(PF_6)_2\cdot CH_3CN$ (**2**) and [Cu(4′-(2-quin)-terpy)Cl](PF_6) (**3**) was carried out according to the procedures given in Scheme 2. To synthesize the complex **1**, a modified two-step literature method was used [29–32]. An equimolar amounts of $[Pt(PhCN)_2Cl_2]$ and $Ag(SO_3CF_3)$ were refluxed in acetonitrile solution to give an intermediate $[Pt(PhCN)_2(CH_3CN)Cl]CF_3SO_3$ which, after filtration of AgCl, was used in the solvatothermal reaction with the *4′-(2-quin)-terpy* ligand. To obtain the compound **2**, $KAuCl_4$ was refluxed with *4′-(2-quin)-terpy* and NH_4PF_6 in methanol:water (1:4 v/v) mixture, while the Cu(II) complex **3** was synthesized using a slow diffusion technique in a test tube, where a solution of $CuCl_2$ with NH_4PF_6 and a solution of *4′-(2-quin)-terpy* ligand were layered on top of each other.

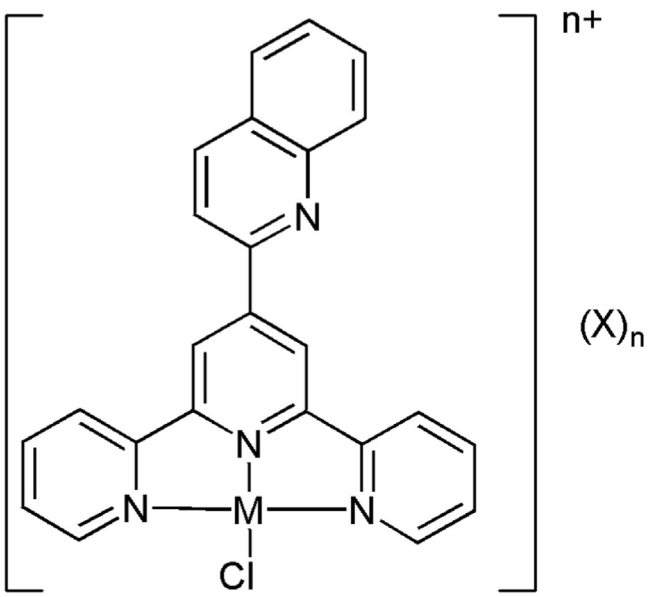

$[M(4'\text{-}(2\text{-quin})\text{-terpy})Cl]^{n+}(X)_n$

Compound	M	X	n
1	Pt	$SO_3CF_3^-$	1
2	Au	PF_6^-	2
3	Cu	PF_6^-	1

Scheme 1. Pt(II), Au(III) and Cu(II) compounds (**1**–**3**) employed in this study.

The compositions of **1**–**3** were established by X-ray analysis in combination with HR-MS spectrometry, FT-IR technique and ^1H and ^{13}C NMR spectroscopy (Figures S1–S4 in ESI[1]). The characteristic absorptions of **1**–**3** originated from stretching vibrations $\nu_{(C=N,\ C=C)}$ occur in the range of 1620–1550 cm^{-1}, and they are slightly increased in energy relative to the free ligands (see Figure S2, ESI[1]). The bands associated with the stretching modes of $CF_3SO_3^-$ counter anion in the IR spectrum of **1** appear at 1263 cm^{-1} ($\nu_a(SO_3)$), 1031 cm^{-1} ($\nu_s(SO_3)$) and 637 cm^{-1} ($\delta_a(SO_3)$) [33], while the intense bands near 840 cm^{-1} and 558 cm^{-1} in the IR spectra of **2** and **3** are indicative of the presence of PF_6^- group [34]. The full assignment of the signals in the ^1H and ^{13}C NMR spectra of the Pt(II) and Au(III) complexes was achieved by using multidimensional techniques ^1H–^{13}C HMBC, ^1H–^{13}C HMQC, ^1H–^1H COSY (Figure S3–S4 in ESI[1]).

2.2. Solid state structures of 1–3

The perspective views of the molecular structures of **1**–**3** together with the atom numbering are depicted in Fig. 1, while the

[1] Electronic Supplementary Information (ESI) available online: HRMS, FT-IR, NMR, XPRD, selected structural data, short intra- and intermolecular interactions, Hirshfeld surface analysis, UV–Vis absorption and stability experiments, UV–Vis spectra upon exposure of reducing agents, the Beer-Lambert law of **1**, Plots of $A_0/(A-A_0)$ vs. 1/[DNA] of UV–Vis CT-DNA titration, CD spectra of control samples, cell viability of cisplatin, Western blot analysis, angiogenic effect of peptide controls.

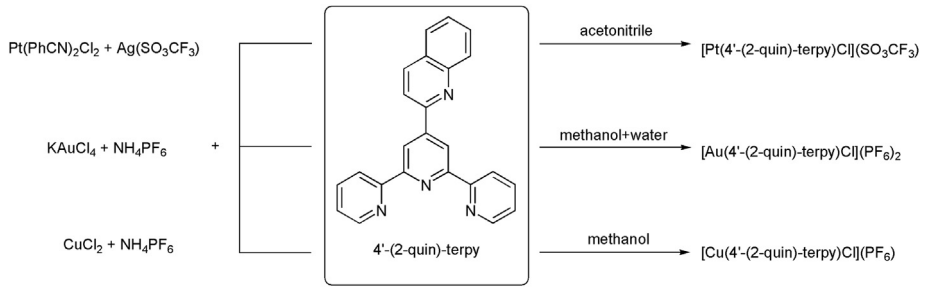

Scheme 2. Synthetic route to compounds **1**–**3**.

selected bond lengths (Å) and bond angles (°) are listed in Table 1.

The metal centre in the $[M(4'\text{-}(2\text{-quin})\text{-terpy})Cl]^{n+}$ (n = 1 for **1** and **3**, n = 2 for **2**) is coordinated by the chloride ion and three nitrogen donors from 4′-(2-quinolinyl)-2,2′:6′,2″-terpyridine ligand, and its coordination sphere is best described as a distorted square planar (Fig. 1). By analogy to the related terpyridine transition metal complexes [35], the $M-N_{central}$ bond length is shorter in relation to those of the outer pyridyl rings (Table 1).

It is worth noting that the square-planar geometry is typical for Pt(II) and Au(III) complexes, but it is highly unusual for terpyridine Cu(II) ones. To the best of our knowledge, $[Cu(4'\text{-}(2\text{-furanyl})\text{-terpy})Cl](CF_3SO_3)$ is an unique example for which the planar conformation has been evident by the X-ray analysis so far [36]. The most common terpyridine Cu(II) structures are $[Cu(4'\text{-R-terpy})Cl_2]$ [37–46] and dimers $[Cu_2(4'\text{-R-terpy})_2Cl_2]X_2$ [47–49] (X = ClO_4^-, PF_6^-), generally possessing Cu(II) ions in square-pyramidal geometry with a long apical bond (in 4 + 1 coordination). In the structure of **3**, the cation $[Cu(4'\text{-}(2\text{-quin})\text{-terpy})Cl]^+$ is ideally coplanar due to the constraints of the *Pnma* space group symmetry. All the atoms occupy the special positions *c* of the *Pnma* space group with the multiplicity four. For **1** and **2**, maximum distances from the best plane defined by the atoms M(1), N(1), N(2), N(3) and Cl(1) are −0.168(15)Å for N(2) in **1** and + 0.015(2)Å for Au(1) in **2**.

The distortion of the complex cations $[M(4'\text{-}(2\text{-quin})\text{-terpy})Cl]^{n+}$ from square planar geometry has been further evaluated using Okuniewski's (τ'_4) parameter [50], defined as (1):

$$\tau'_4 = \frac{\beta - \alpha}{360^\circ - \theta} + \frac{180^\circ - \beta}{180^\circ - \theta} \quad (1)$$

where α and β are two greatest valence angles (α < β) and $\theta = \cos^{-1}\left(-\frac{1}{3}\right) \approx 109.5^\circ$.

Table 1
Selected bond lengths [Å] and angles [°] of complexes **1**–**3**.

Bond length	1 (M = Pt)	2 (M = Au)	3 (M = Cu)
M(1)–Cl(1)	2.3046(10)	2.2563(19)	2.1835(16)
M(1)–N(1)	2.016(4)	2.028(6)	2.034(5)
M(1)–N(2)	1.934(3)	1.955(5)	1.934(4)
M(1)–N(3)	2.010(4)	2.009(6)	2.033(5)
Bond angle	**1** (M = Pt)	**2** (M = Au)	**3** (M = Cu)
N(1)–M(1)–Cl(1)	99.21(9)	98.17(16)	101.12(14)
N(2)–M(1)–Cl(1)	178.75(10)	178.25(16)	179.24(14)
N(3)–M(1)–Cl(1)	98.51(9)	100.10(18)	99.61(13)
N(1)–M(1)–N(2)	81.45(14)	80.4(2)	79.64(18)
N(1)–M(1)–N(3)	162.28(13)	161.7(2)	159.27(18)
N(2)–M(1)–N(3)	80.83(14)	81.3(2)	79.63(18)

For ideal square planar and tetrahedral structures, τ'_4 parameters are expected to take values of 0 and 1, respectively. Consistent with the calculated τ'_4 values, the deviation from square planar geometry around the central atom in $[M(4'\text{-}(2\text{-quin})\text{-terpy})Cl]^{n+}$ increases in the order **1** (τ'_4 = 0.053) < **2** (τ'_4 = 0.056) < **3** (τ'_4 = 0.060). The angular distortion of the $[M(4'\text{-}(2\text{-quin})\text{-terpy})Cl]^{n+}$ unit from the idealized geometry is attributed to the presence of the *4′-(2-quin)-terpy* ligand, which acts as chelating tridentate and forms two fused five-member chelate rings. The N(2)–M(1)–N(1) and N(2)–M(1)–N(3) angles vary in the range 79.63–81.45°, while the N–M–Cl angles are between 98.17 and 101.12° (Table 1). All they deviate from 90° expected for a square planar geometry. In the case of **1**, the *terpy* framework is approximately planar, with the dihedral angles between the mean planes of the central pyridine and terminal aromatic rings equal 3.4(1)° and 3.5(1)°, while *2-quin* unit is inclined at 26.0(1)° to the central pyridine. Remarkably, in **2** and **3**, the whole *4′-(2-quin)-terpy* ligand adopts a planar structure.

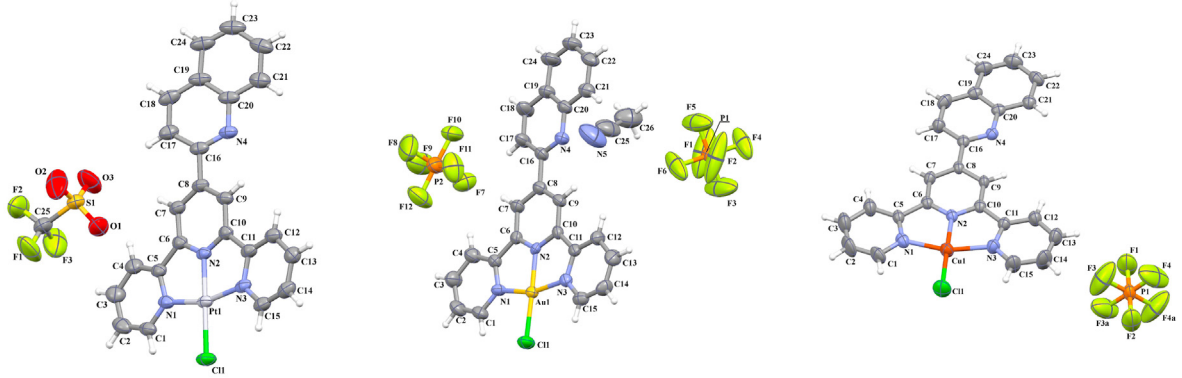

1 **2** **3**

Fig. 1. The molecular structures of **1**–**3** together with the atom numbering. Displacement ellipsoids are drawn at 50% probability level.

The dihedral angle between the central pyridine and peripheral pyridyl ring is 2.4(3)° in **2** and 0° in **3**, while the dihedral angle between the central pyridine and *2-quin* substituent equals to 3.2(3)° in **2** and 0° in **3** (Table S1, ESI[1]). The ligand planarity is beneficial in the context of possible intercalative interaction of the complex with DNA due to π-stacking between the plane of the aromatic rings and DNA base pairs.

The differences concerning the twisting of the pendant heterocycle subsistent in relation to central pyridine ring in **1**–**3** seem to be a consequence of the crystallographic symmetry and crystal packing effects. As shown in Fig. 2 and ESI materials[1] (Figure S6 and Tables S2–S4), the packing arrangements for **1**–**3** demonstrate a large contribution of π···π interactions in all the structures as well as Cl···π (in **1**), C–H···F, C–H···N and C–H···Cl (in **2** and **3**).

In **1** and **3**, the neighbouring cations $[M(4'\text{-}(2\text{-quin})\text{-terpy})Cl]^+$ are stacked in a head-to-tail orientation with two alternating distances 3.3903(2) and 3.7139(2) Å between adjacent complexes in **1** and one spacing of 6.6271(0) in **3**. The Pt···Pt distances below 3.5 Å are indicative for effective metallophilic (d_z^2–d_z^2 orbital) interactions [17,51,52]. As shown by Hirshfeld surface analysis [53–55], Pt···Pt interactions covers 1.1% of all the surface contacts (see ESI[1], Figures S7 and S8). In the structure **2**, two fluorine atoms (from two different hexafluorophosphate anions) are weakly bonded to the Au(III) ions, occupying the axial coordination sites (Figure S9, ESI[1]). The formed Au–F distances of 3.031(9) and 2.883(8) Å are shorter than the sum of van der Waals radii of gold and fluorine (3.13 Å) [56,57], giving rise to a pseudo-octahedral coordination around gold(III) in **2** as in the previously reported $[AuCl(4'\text{-}R^1\text{-terpy})](PF_6)_2$ [58], $[AuCl(4'\text{-}R^2\text{-terpy})](PF_6)_2$ [58], $[AuCl(terpy)](BF_4)_2$ [59], $[Au(C_6F_5)(\eta^3\text{-terpy})](PF_6)_2$ [57], $[Au(bpMe)Cl_2][PF_6]$ [60], $[Au(bpOMe)Cl_2][PF_6]$ [60], $[AuCl(bmpa\text{-}H)](BF_4)$ [61] and $[Au(R\text{-pyoxPh})Cl_2][PF_6]_{0.5}[AuCl_4]_{0.5}$ [62]. In **3**, the shortest distance between the Cu(II) ion and fluorine atom of hexafluorophosphate anions is 4.702(0) Å.

2.3. UV–vis spectroscopy studies

The electronic absorption spectra of **1**–**3** (5×10^{-5} M) were collected in CH_3CN, DMSO and 10 mM phosphate buffered saline (PBS, pH 7.4) once every 4 h over 48 h at room temperature (Figures S10–S14 and Table S5 in ESI[1]). For all the complexes, strong absorptions in the high-energy region (250–350 nm) are attributed to π→π* and n→π* intraligand (IL) transitions within the coordinated terpyridyl ligand. Low energy absorption bands (350–450 nm) in the spectra of **1** and **2** are attributed to metal-to-ligand charge-transfer (MLCT) [31,63–68] and ligand-to-metal charge-transfer (LMCT) [57,69–73], respectively. For Cu(II) complex (**3**), the weak band at ~700 nm originates from spin-allowed $d_{xy}\rightarrow d^{22}_{x\text{-}y}$, d_{yz}, $d_{xz}\rightarrow d^{22}_{x\text{-}y}$ and $d^2_z\rightarrow d^{22}_{x\text{-}y}$ copper(II) transitions [74–76] (Figures S10–S11 in ESI[1]).

Except for **1** in PBS and **2** in DMSO, there was no change in the absorbance profile of the designed complexes over 48 h, indicating their stability in solution (Fig. 3 and Figures S12–S14 in ESI[1]). PBS solution of **1** (5×10^{-5} M) shows a noticeable broad absorption band at 488 nm, which can be attributed to metal-metal-to-ligand charge-transfer (MMLCT; $d\sigma^*(Pt_2)\rightarrow\pi^*(terpy)$] transitions arising from the presence of Pt···Pt and/or π–π stacking interactions, favoured in polar environment. The observed suppression of absorbance intensity of PBS solution of **1** in the entire spectral range is thus a consequence of aggregation process, as evidenced by the deviation from the Beer-Lambert Law for highly concentrated solutions of **1** (Figure S15, ESI[1]) [77–81]. In the case of solution with lower concentration of **1** (5×10^{-6} M), the MMLCT absorption disappears and the absorbance bands remain constant over 48 h (Figure S12, ESI[1]). Also, addition of DMSO to the PBS solution of **1** leads to a decrease of MMLCT absorbance intensity (Figure S16, ESI[1]).

Stability experiments for compound **2** in DMSO revealed a decrease in the intensity of the LMCT, most likely due to chloride-DMSO exchange reaction, in agreement with the results reported for gold(III) complexes bearing hydroxyl- and amino-quinoline ligands [82]. However, the partial hydrolysis of the complex cation $[Au(4'\text{-}(2\text{-quin})\text{-terpy})Cl]^{2+}$ cannot be excluded [83].

Upon addition of the stoichiometric amount of glutathione or sodium ascorbate (reducing agents abundant in most cancer cells cytoplasm) to buffer solutions of **1**–**3**, only UV–Vis spectra of **3** remain unaltered (supplementary[1] Figure S17). The stability of **1** and **2** is strongly diminished by the reducing agents, as reflected by rapid changes in their absorbance profile, with loss of the LMCT/MLCT bands. Lack of the formation of absorbance typical of colloidal gold(0) between 500 and 600 nm in UV–Vis spectrum of **2** upon exposure of glutathione and sodium ascorbate may signal conversion from gold(III) to gold(I) [84,85].

2.4. DNA binding

Complex **1** has a higher inclination of the 2-quin unit (26.0(1)°) to the central pyridine when compared to complex **2** and complex **3** [3.2(3)° and 0°, respectively] (Table S1 in ESI[1]). As planarity of ligands might affect interaction of complexes with their targets, namely DNA [16], we further studied the *in vitro* interaction between our complexes and calf-thymus DNA (CT-DNA). To study the mode of interactions between DNA and complex molecules, three different instrumental techniques were used, that are UV–Vis absorption titration, ethidium bromide displacement assay and circular dichroism spectroscopy.

2.4.1. UV–vis spectrophotometric DNA titration

In this method, drug–DNA interactions are studied by comparison of UV–Visible absorption spectra of the free drug and drug–DNA complexes. Compounds which bind with DNA through intercalative mode concerning a stacking interaction between the planar aromatic chromophore and the base pairs of DNA usually results in hypochromism, along with or without a small red shift in the wavelength. The hyperchromic effect is associated with the external contact (electrostatic binding) or to the major/minor grooves of the DNA [6,7,86–91].

As depicted in Fig. 4, the addition of increasing amounts of CT-DNA to the solution of **2** in PBS (25 μM) results in a decrease in the absorption intensity of the MLCT band at 357 nm. On the contrary, the intraligand (IL) absorbance at 282 nm shows hyperchromism up to r = 5 (where *r* is the [DNA]/[complex] mixing ratio), and upon further addition of CT-DNA, the band intensity is decreasing. Such observations may indicate the presence of different modes of interactions between DNA and complex molecules. The hyperchromic effect is most probably due to the presence of charged cations which bind to DNA via electrostatic attraction to the phosphate group of the DNA, while hypochromism is indicative for intercalative binding [6,7,86–91]. Notably, the second effect seems to be strongly preferred at higher DNA concentrations. The dual-function mode of action of **2** is also supported by the isosbestic point at 333 nm disappearing for [DNA]/[**2**] > 5, and it is reflected in a clear deviation from linearity $A_0/(A\text{-}A_0)$ vs. 1/[DNA] plot for the absorbance data at 357 nm [88]. The intrinsic binding constant K_b of **2**, estimated from the intercept to-slope ratio of $A_0/(A\text{-}A_0)$ vs 1/[DNA] plot was 1.20×10^4 M^{-1}.

Different modes of interactions with DNA are clearly shown also in the case of the complex **1** in PBS (5 μM). The hypochromism of the absorption bands at 330 and 283 nm, isosbestic points at 409 and 359 nm and appearance of new band at 436 nm, are indicative

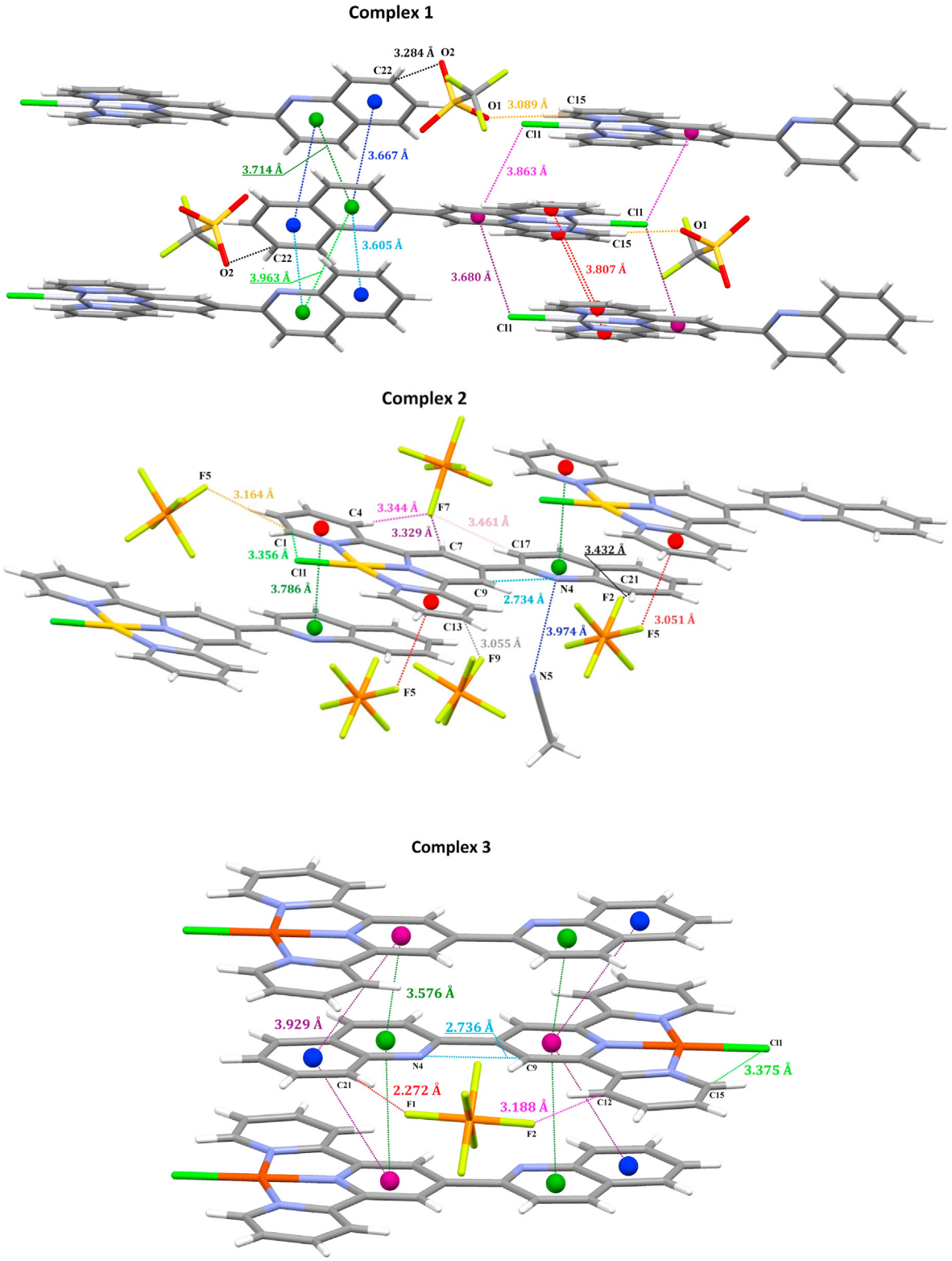

Fig. 2. View of the supramolecular packing of complexes **1**–**3**.

for the presence of both the stacking interaction between the planar aromatic chromophore and the base pairs of DNA and covalent interaction via the loss of the chloride ions [6,7,86–91].

The addition of increasing amounts of CT-DNA to the solution of **3** in PBS (25 μM) results in a decrease in the absorption intensity of both CT and IL bands at 332 and 279 nm, which could suggest intercalation mode of binding. However, a clear deviation from linearity $A_0/(A- A_0)$ vs. 1/[DNA] plot for the absorbance data at 332 nm is indicative for presence of different interactions between the complex molecules and DNA (Figure S18 in ESI[1]).

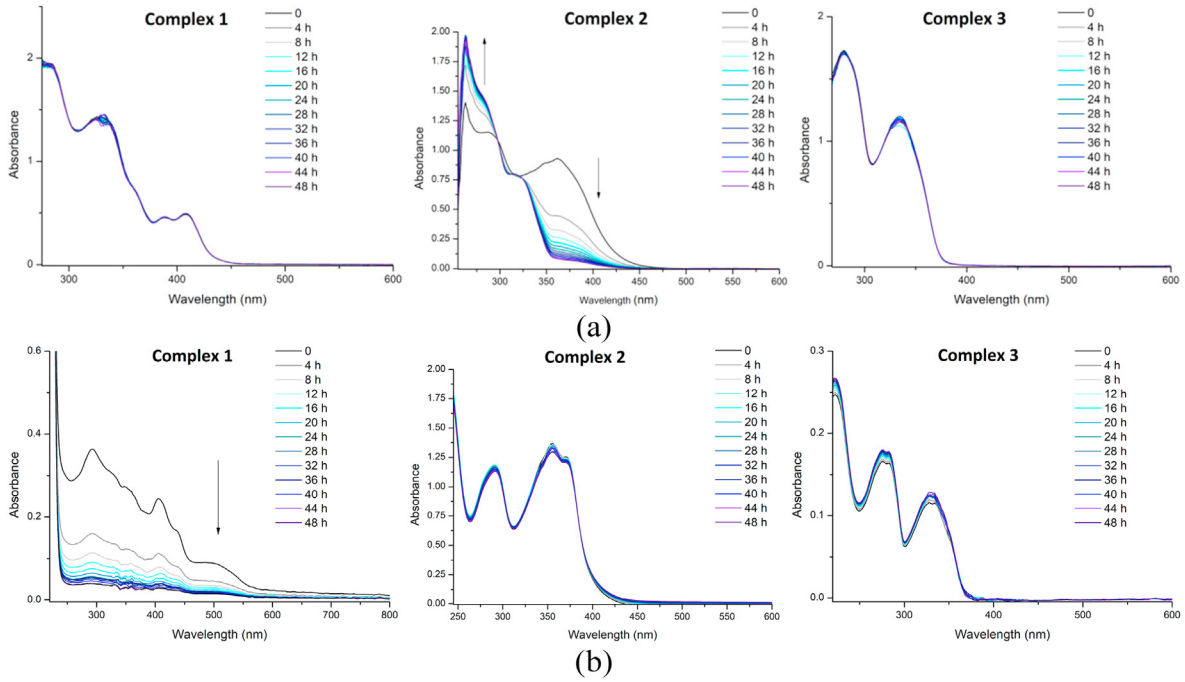

Fig. 3. UV–Vis spectra **1**–**3** in DMSO (a) and PBS (b) (5×10^{-5} M) recorded once every 4 h over 48 h at room temperature.

2.4.2. Ethidium bromide displacement assay

Ethidium dibromide (EB) is a standard intercalating agent. Due to strong interactions between ethidium bromide and adjacent DNA base pairs, EB shows the enhanced fluorescence in the presence of DNA. Any compound that intercalates into DNA equally or more strongly than EB replaces it from the EB-DNA adduct, leading to decrease or quenching of the fluorescence emission [92]. Binding interaction of **1**–**3** to CT-DNA was estimated using ethidium bromide (EB) displacement assay in PBS buffer with the constant concentration of CT-DNA and EB ([DNA] = [EB] = 50 μM) and varying the concentrations of the complexes.

The changes in the fluorescence intensity of EB–CT-DNA adduct with increase of concentrations of the tested compounds **1**–**3** are shown in Fig. 5. All the three complexes show no emission in this region.

For each complex, fluorescence intensity decreases as the compound concentration increases, indicating that EB molecules are displaced from their DNA binding sites and replaced by the appropriate complex. The complexes **1**, **2** and **3** quenched 33%, 58% and 14% of the fluorescence of the EB–CT-DNA adduct, respectively.

The calculated DNA binding constants (Table S6 ESI[1]) were found to increase in the order **3** ($K_{app} = 1.53 \times 10^6$ M^{-1}) < **1** ($K_{app} = 5.71 \times 10^6$ M^{-1}) < **2** ($K_{app} = 3.45 \times 10^7$ M^{-1}), indicating that complex **2** competes with EB bound to CT-DNA much more efficiently than **1** and **3**. The lack of the strong correlation with the tendency observed for the binding constants K_b (Table S6) can be explained by the simultaneous presence of different modes of interactions between DNA and longer incubation time in EB displacement assay, which seems to encourage the intercalative mode of binding.

2.4.3. Circular dichroism spectroscopy

To take further insights into the nature of the interactions of complexes with DNA, a circular dichroism analysis was performed using calf thymus DNA (CT-DNA) in the presence of the increasing concentrations of the complexes or in the presence of DMSO (control). With this technique it is possible to detect conformational alterations of DNA using circularly polarized electromagnetic light (Fig. 6) [93].

The circular dichroism spectra of the B-form of CT-DNA presents a negative peak at 245 nm, correlated with the right-handed helicity of DNA, and a positive peak at 275 nm, due to base-pair stacking [93,94]. The incubation of CT-DNA with increasing concentrations of the three complexes results in a change of intensity and/or profile of both CD bands (Fig. 6). A hypochromic effect is generally correlated with intercalation of ligands causing the elongation of the double helix [93,95], which can be observed for all complexes for the 275 nm peak. Interestingly, CD of CT-DNA incubated with 25 μM of complex **3** presents a positive peak at 245 nm accompanied by a slightly negative peak near 280 nm, which are more typical of Z-form of DNA (Fig. 6C). CT-DNA incubated with 25 μM of complex **1** displays CD spectra with the loss of the 275 nm positive peak while maintaining the 254 nm peak, while CT-DNA incubated with 25 μM of complex **2** presents both peaks (Fig. 6A and B). Additionally, an extrinsic CD with different amplitudes is also observed in CT-DNA – complexes spectra's around 350–390 nm for **3** (more pronounced) and **2** and 350–450 nm for **1**, respectively (Fig. 6). Since complexes **1, 2** and **3** do not have a significant CD activity at these wavelength range (Supplementary[1] Figure S19), these peaks are probably the result of the interaction between complexes and CT-DNA. The appearance of this extrinsic CD peak was correlated with the intercalation of ligand to DNA [96]. These results suggest that the secondary structure of DNA is efficiently destabilized by all the three complexes (Fig. 6). Nevertheless, complex **3** seem to induce a higher destabilization compared to the other complexes, which might be correlated with the planarity of ligand in **3**.

Despite complex **2** competes with EB bound to CT-DNA much more efficiently than **1** and **3**, after a 30 min incubation (Fig. 5), it seems that a longer incubation period (6 h) might influence CT-DNA structure in a different manner (Fig. 6). Nevertheless, our CD results agree that all complexes can interact *in vitro* with CT-DNA (Figs. 4 and 5), but complex **3** induces an increased change in the helicity of DNA (conversion of a right to a left-handed form).

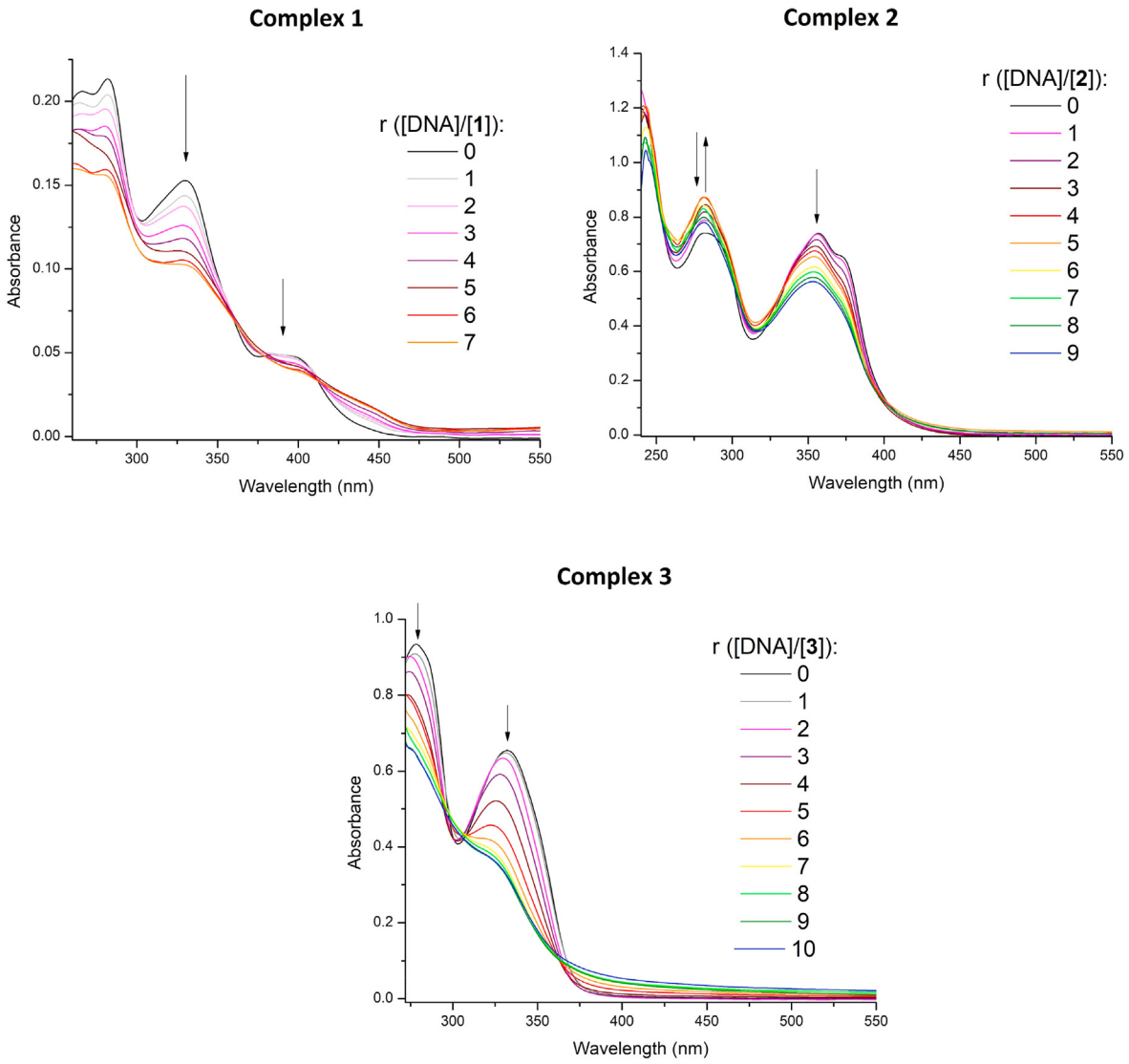

Fig. 4. UV−vis spectra of PBS solution of complex **1** (5 μM), **2** (25 μM) and **3** (25 μM) in the absence and presence of increasing amounts of CT-DNA. The arrows show the changes upon increasing amounts of CT-DNA.

2.5. Biological activity

Next, we decided to evaluate the biological effect of the complexes within human cells. Considering that, the antiproliferative effect of the complexes **1**–**3** was determined in two cancer cells, A2780 (derived from ovarian carcinoma) and HCT116 (derived from colorectal carcinoma) and in normal dermal fibroblasts using the MTS assay after a 48 h incubation (Fig. 7). It is possible to observe a concentration dependent decrease in cellular viability of complexes **1**–**3** (Fig. 7).

The highest cytotoxic effect was displayed by complex **3** (lower IC_{50}) in the HCT116 cell line (Fig. 7 and Table 2). The cytotoxicity of the complexes follows the trend **3** > **2** > **1** in the three cell lines studied (Fig. 7 and Table 2), despite the IC_{50} values in colorectal cancer cells seem to be more similar for all complexes compared to the IC_{50} values observed in A2780 cells or in normal fibroblasts. Indeed, complexes **2** and **3** are much more cytotoxic to A2780 and fibroblasts compared to complex **1** (Table 2).

Nevertheless, all three complexes showed higher cytotoxicity in HCT116 cancer cell line and lower cytotoxicity in normal dermal fibroblasts (Fig. 7 and Table 2). Particularly, complex **1** seems to be the less cytotoxic to normal cells (IC_{50} > 100 μM). Using similar *terpy* frameworks, previously published Au(III) complexes displayed higher cytotoxicity than similar Cu(II) and Pt(II) complexes, while in this work, complex **3,** a Cu(II) complex, displayed higher cytotoxicity than its Au(III) counterpart, complex **2** (Fig. 7 and Table 2). Our results also seem to support previous published works, in which the *terpy* framework displays higher cytotoxicity in HCT116 cell line when compared to A2780 cancer cell line and normal dermal fibroblasts [97,98].

The lower solubility of complex **1** in PBS may contribute to its lower cytotoxicity (Figs. 3 and 7, Table 2); however, we have observed a decrease of cell viability with the increase of complex **1** concentration (Fig. 7). Importantly, differences in cytotoxicity appear to reflect deviations from planar symmetry of the complexes. Complex **1**, which displays lower cytotoxicity, has a higher inclination of the *2-quin* unit (26.0(1)°) to the central pyridine when compared to other complexes (Fig. 7, Table 2 and Table S1 in ESI[1]). Interestingly, the differences in the cytotoxicity displayed by complexes **2** and **3** also appear to follow the inclination of *2-quin* unit towards the central pyridine [3.2(3)° and 0°, respectively] (Fig. 7, Table 2 and Table S1, ESI[1]). The planarity of the ligands could

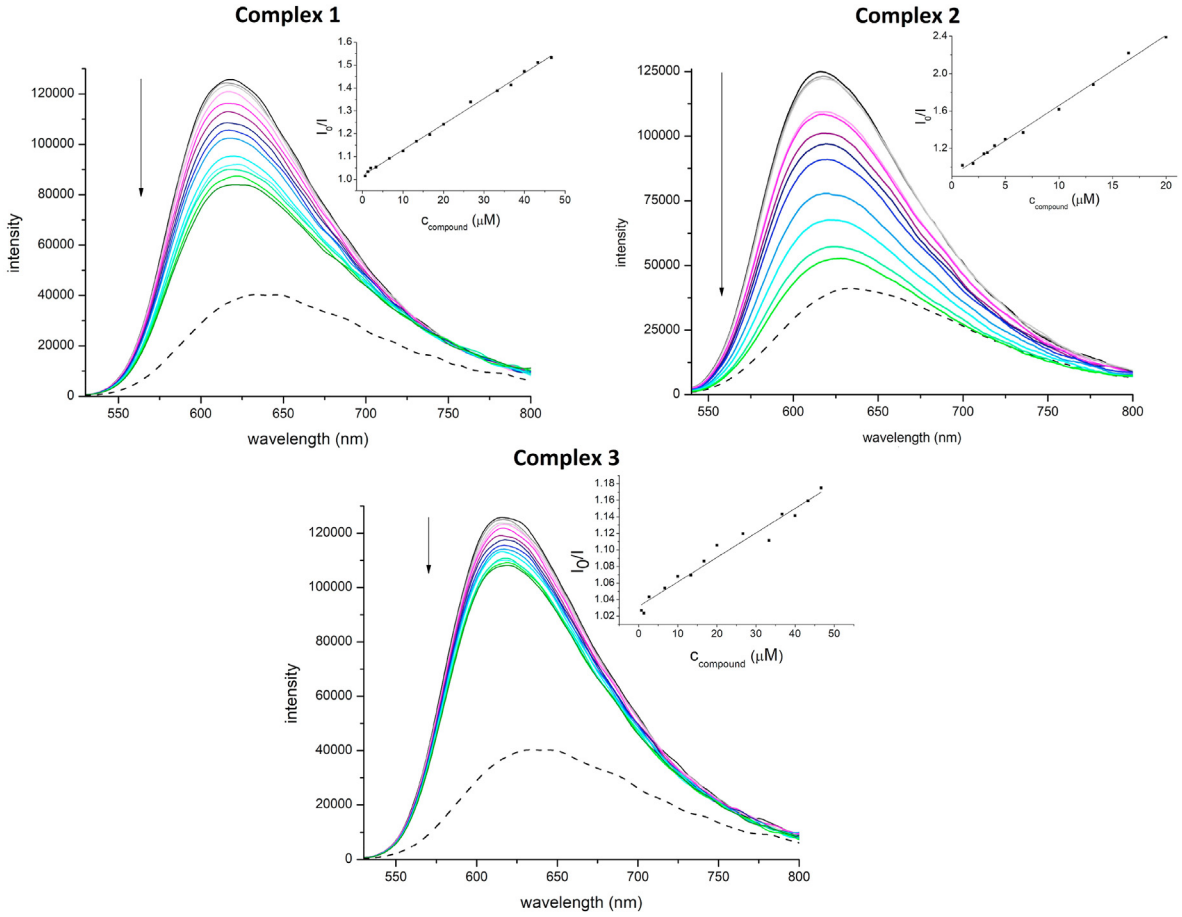

Fig. 5. Emission spectra (λ_{ex} = 510 nm) of EB–CT-DNA in PBS buffer with the increasing concentration of **1**–**3** (0–50 μM for **1**, **3** and 0–20 μM for **2**). The inset shows the Stern-Volmer plots for corresponding complexes.

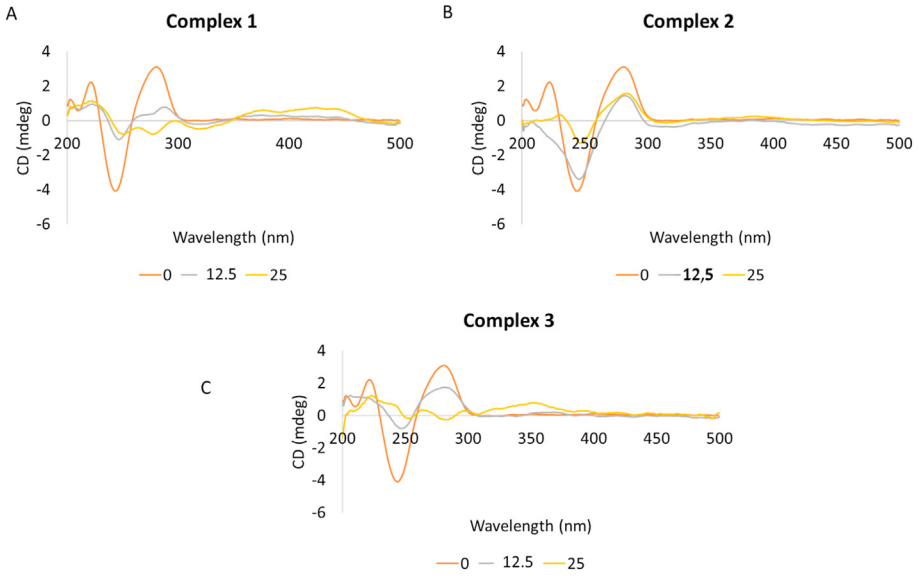

Fig. 6. CD-spectra of CT-DNA (12.5 μM) incubated for 6 h at 37 °C with increasing 0, 12.5 and 25 μM of complex **1** (A), **2** (B) or **3** (C). Results were normalized to vehicle controls (DMSO 0% 2.5% and 5%, respectively).

affect the cytotoxicity of the complexes by affecting their ability to interact with some of their targets, namely DNA. Indeed, when we analyze the results from CD it seems that after intercalation complex **3**, the planar one and the one demonstrating a more cytotoxic effect (Fig. 7), induces a higher destabilization of the double helix (Fig. 6). The results presented in Figs. 4–6 suggest that

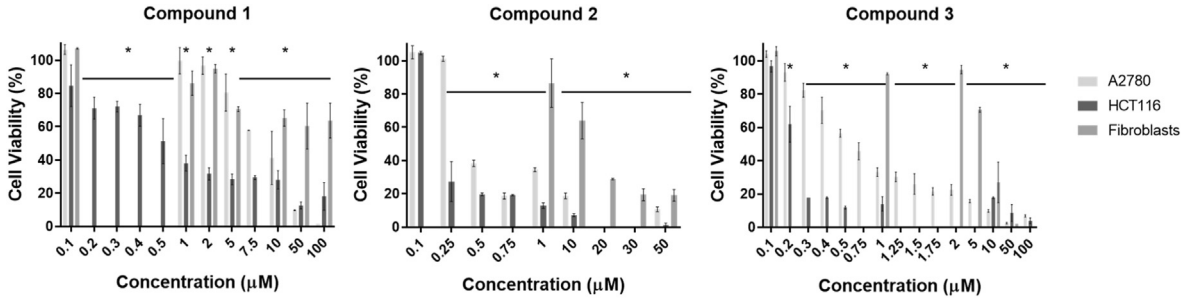

Fig. 7. Antiproliferative effect of complexes **1**–**3** in A2780 and HCT116 cancer cell lines and in normal dermal fibroblasts determined by the MTS assay. DMSO 0.1% was used as a vehicle control. The results are presented as mean ± SD of three independent assays. The symbol * indicates a p-value < 0.05.

Table 2
Relative IC_{50} values (μM) of complexes **1**–**3** in A2780 and HCT116 cancer cell lines and in normal dermal fibroblasts.

Cell lines	1 (μM)	2 (μM)	3 (μM)
A2780	7.12 ± 0.92	0.38 ± 0.06	0.37 ± 0.08
HCT116	0.61 ± 0.06	0.24 ± 0.12	0.21 ± 0.07
Fibroblasts	IC_{50} > 100	14.34 ± 0.57	7.2 ± 0.96

DNA intercalation by complexes **1**, **2** and **3** could be important for the cytotoxicity displayed by the complexes (Fig. 7 and Table 2). We should always be careful when correlating *in vitro* and cell-based assay. Indeed, we analysed the effect of complexes in CT-DNA *in vitro* (without cells). In a complex media/environment such as cells, more interactions with different targets might exist, meaning that the amount of complex reaching the nucleus might be too low to see a real effect on DNA. Nevertheless, the higher stability of complex **3** in the presence of reducing agents (as cytoplasm is a more reducing environment) may contribute to reach its biological target (namely DNA) more easily and the slightly higher cytotoxicity when compared to complex **2** (Fig. 7 and Figure S17, ESI[1]). Considering all this cell-associated complexity it is important to further understand the differential cytotoxicity displayed by complexes **1**, **2** and **3** in HCT116 cell line. The internalization of complexes within cells is also an important point to consider as the % of complexes internalized in cells might correlate with their cytotoxicity. In that respect, HCT116 cells were incubated with the three complexes for 4 h at two different temperatures, 4 °C and 37 °C, and inductively coupled plasma atomic emission spectrometry (ICP-AES) used to quantify the % of metal in the cellular fraction (cells incubated with complexes compared to cells in the absence of complexes (Fig. 8). Since copper is an essential metal normalization of results to cells copper levels in the absence of complex **3** is important. It is important to note also, that due to the low IC_{50} of the complexes and the sensitivity of ICP-AES technique, a higher concentration of complexes **1**–**3** (20× IC_{50}) was used (ensuring measurable amounts of Pt, Au and Cu by ICP-AES). Due to the high toxicity associated with the exposure of cells for 48 h to these concentrations, internalization was assessed after a 4 h incubation time (Fig. 8).

When we observe the % of normalized intracellular Pt, Au and Cu at 37 °C a correlation of internalization and cytotoxicity is clearly observed with **3** > **2** > **1** (Figs. 7 and 8). Indeed, at 37 °C, 13%, 26% and 33% of complex **1, 2** and **3,** respectively is observed in cells (Fig. 8). Interestingly, when we performed the same assay but at 4 °C (a reduction of cell metabolic activity and energy dependent uptake is observed) there is a significative reduction of the intracellular % of **1** and **3** (13%–7% for complex **1**, and 33%–18% for complex **3**) (Fig. 8). On the contrary, for complex **2** no effect in the % of internalization is observed when we reduce the temperature of

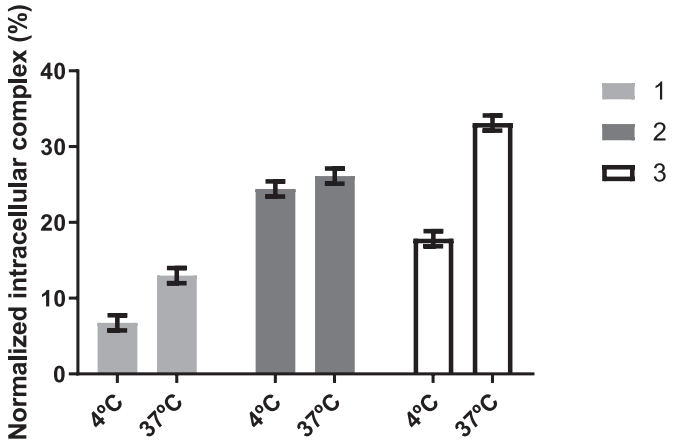

Fig. 8. Internalization of complexes **1**–**3** as evaluated by ICP-AES determination of Pt, Au and Cu, respectively, in the cellular fraction of HCT116 cancer cells after 4 h exposure of cells to 20× the respective IC_{50} concentrations at 4 °C and 37 °C. Results were normalized to the DMSO control and to the respective complex concentration added to cells.

incubation (Fig. 8). These results might indicate that **2** might enter cells via an energy-independent process, while **1** and **3** enter cells mediated in part by an energy-dependent process (Fig. 8).

Considering that in our experimental conditions, the IC_{50} of cisplatin in HCT116 and A2780 cell lines is 15.4 and 3.4 μM, respectively (supplementary[1] Figure S20), the complexes here described deserved great attention due to the low IC_{50}, particularly in HCT116 cell line. Indeed, other published metallic complexes with terpyridine ligands display IC_{50} values in the range of 0.3–17.3 μM in the HCT116 cell line while in the A2780 cell line IC_{50} values vary from 0.95 to 16.2 μM when effective [46,97,98]. The complexes here described have IC_{50} within the lower range of the interval for the HCT116 cell line (Fig. 7, Table 2). Therefore, this cell line was chosen to further characterize the biological mechanisms involved in the observed loss of viability induced by complexes **1**–**3**.

2.5.1. Apoptosis induction after exposure of HCT116 cells to IC_{50} concentrations of complexes 1-3

The loss of cell viability observed in the presence of complexes **1**–**3** deserved further exploitation and cell death process was further studied. As a first approach, apoptosis, a programmed cell death, was determined by flow cytometry using the Annexin V-Alexa fluor 488/PI double staining after 48 h of exposure of HCT116 cells to IC_{50} concentrations of complexes **1**–**3** (Fig. 9).

With this method, it is possible to distinguish cells in early apoptosis (labelled with Annexin V-Alexa fluor 488 stain only), cells

in late apoptosis (labelled with both Annexin V-Alexa fluor 488 and PI stains), cells in necrosis (labelled with PI stain only) from normal viable cells (not labelled with any of the stains). It is possible to observe a statistically significant increase in apoptotic cells exposed to complex **3** in both early and late apoptosis (Fig. 9). There is an 6.5 × increase of apoptotic cells (both early and late) in HCT116 cells exposed to compound **3** when compared to the DMSO control (2.85% and 0.44%, respectively) (Fig. 9) Exposure to the other complexes revealed a non-statistically increase in apoptotic HCT116 cells, 0.67% and 0.55%, respectively. Induction of apoptosis was also observed in other complexes bearing *terpy* ligands [97,98]. There was also a small decrease of HCT116 cells in necrosis, although not statistically significant, in cells exposed to complex **1** (1.91%), complex **2** (2.15%) and complex **3** (1.56%) when compared to the cells exposed to the DMSO control (2.49%) (Fig. 9).

2.5.2. Determination of BAX and BCL-2 protein expression by western-blot

As a good marker of apoptosis induction is the increase in the ratio of pro-apoptotic protein BAX versus anti-apoptotic protein BCL-2 [99]. Considering that, HCT116 cells were exposed to IC_{50} concentrations of the complexes for 48 h and the levels of the pro-apoptotic protein BAX and the anti-apoptotic protein BCL-2 were determined by western-blot (WB) (Fig. 10 and Figure S21).

Our results show a statistical increase of the BAX/BCL-2 ratio for the three complexes (Fig. 10C), in agreement with the induction of apoptosis in Fig. 9. Despite we were expecting a higher ratio BAX/BCL2 for complex **3,** it should be mentioned that despite both methods are evaluating the trigger of apoptosis, they target different features in the whole the process. Indeed, flow cytometry allow us to quantify phosphatidylserine on the external cell membrane (translocation triggered in early phases of apoptosis) (Fig. 9) while WB were used to quantify the levels of BAX and BCL-2 (pro-apoptotic and anti-apoptotic proteins, respectively) that are involved in the control of mitochondrial membrane permeability [99]. Under stress conditions, cytoplasmatic BAX undergoes a conformational change that causes its translocation to the mitochondrion outer membrane and trigger pore formation and release of cytochrome C into the cytoplasm an event that precedes activation of caspases [99]. Moreover, recently, in a study describing novel oxovanadium complexes, cellular detachment, probably due to membrane destabilization, was identified as a contributing factor to underestimate apoptosis when using Annexin V-Alexa fluor 488/PI assay by flow cytometry [100]. We cannot discard that this may also be occurring with cells exposed to complexes **1**–**3** for 48 h and another reason for the small values discrepancies between methods.

Since the induction of apoptosis, via this intrinsic pathway, is associated with a destabilization of mitochondrial membrane potential, we subsequently evaluated the effect of the complexes on mitochondrial membrane potential.

2.5.3. Evaluation of the mitochondrial membrane potential ($\Delta\Psi M$) changes

To evaluate the integrity of the mitochondrial membrane, changes in its membrane potential were evaluated using the cationic dye JC-1 that as a monomer exhibits green fluorescence. The negative potential of the inner mitochondrial membrane (high $\Delta\Psi M$) induces aggregation of the JC-1 dye within mitochondria and results in a red shift of the dye's fluorescence (from 532 to 590 nm). Therefore, cells with permeable mitochondria will display a lower red/green fluorescence ratio.

The results show a significant dissipation of the mitochondrial membrane potential in HCT116 cells exposed to the complexes **1**–**3** for 48 h (Fig. 11), These results agree with previous data from BAX/BCL2 ratio (Fig. 10) and that exposure to complexes **1**–**3** trigger apoptosis through the intrinsic pathway [99].

2.5.4. Autophagy induction after exposure of HCT116 cells to IC_{50} concentrations of complexes 1-3

Considering the high cytotoxicity induced by the complexes we were expecting a higher level of cell death. Besides apoptosis other types of programmed cell death have been described, namely autophagy. Autophagy has been implicated with cytotoxicity associated with cisplatin and novel vanadium and platinum coordination complexes [100,101]. The induction of autophagy in HCT116 cell line after exposure to complexes **1**–**3** was investigated, by the identification of cells carrying autophagosomes after 48 h exposure to IC_{50} concentrations of the complexes (Fig. 12).

There is an increase in the autophagic HCT116 cells due to exposure to complexes **1**–**3**, when compared to the DMSO 0.1% control, (Fig. 12). Complexes **1**, **2** and **3** presented 4.4%, 9.3% and 14.0% of cells in autophagy, respectively, which represent increases of 2.6 × , 5.5 × and 8.2 × when compared with autophagic cells in the DMSO control (1.7%) (Fig. 12). The level of autophagy induced by complex **3** was almost similar to the level induced by rapamycin, the positive control (Fig. 12). The autophagic cell death agrees with the cytotoxicity of complexes (Fig. 7 and Table 2), apoptosis by flow cytometry (Fig. 9) and internalization (Fig. 8) with **3** > **2** > **1**.

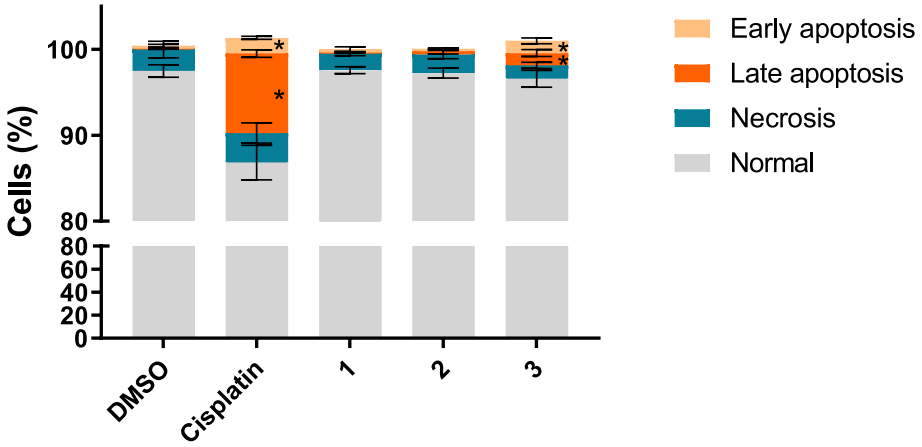

Fig. 9. Induction of apoptosis in HCT116 cells exposed to IC_{50} concentrations of complexes 1–3 for 48 h evaluated by flow cytometry using the Annexin V/PI double staining. DMSO 0.1% (v/v) and cisplatin 15.4 μM were used as vehicle and positive controls, respectively. The results are presented as mean ± SD of three independent assays. The symbol * indicates a p-value < 0.05.

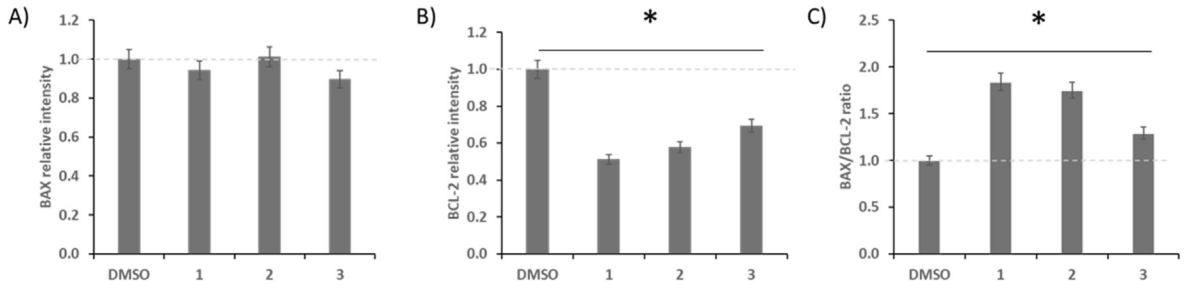

Fig. 10. Expression of BAX (A) and BCL-2 (B) proteins in HCT116 cells incubated for 24 h with complex **1**, **2**, **3** or 0.1% (v/v) DMSO (control). (C) Apoptotic index of HCT116 cells, calculated by BAX/BCL-2 ratio. The symbol * indicates a p-value < 0.05.

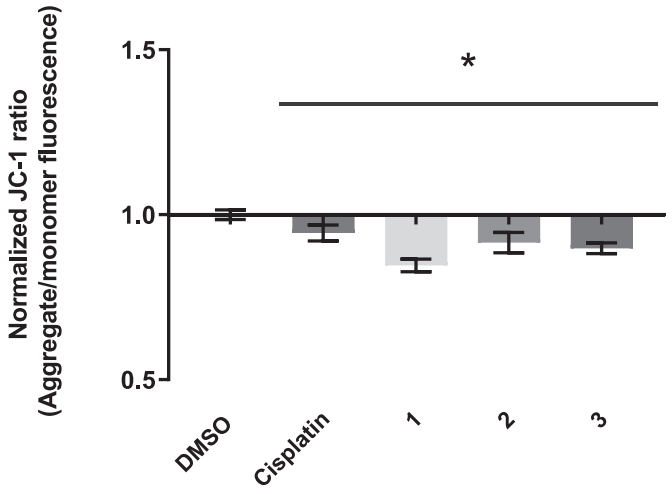

Fig. 11. Evaluation of mitochondrial membrane potential membrane (ΔΨM) changes in HCT116 cells exposed to IC_{50} concentrations of complexes **1**–**3** for 48 h evaluated by flow cytometry using JC-1 staining. DMSO 0.1% (v/v) and cisplatin 15.4 μM were used as vehicle and positive controls, respectively. The aggregate (red fluorescence)/monomer (green fluorescence) ratios were normalized for the DMSO control ratio. The results are presented as mean ± SD of three independent assays. The symbol * indicates a p-value < 0.05.

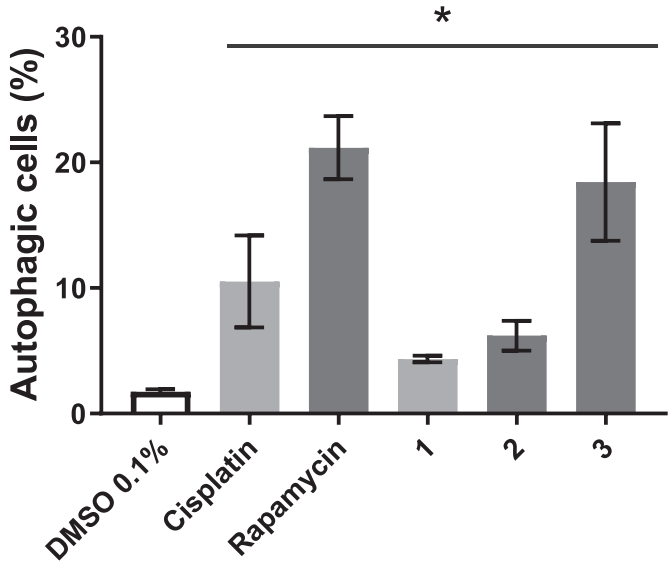

Fig. 12. Induction of autophagy in HCT116 cells exposed to IC_{50} concentrations of complexes **1**–**3** for 48 h evaluated by flow cytometry using the Autophagy assay (Abcam). DMSO 0.1% (v/v) was used as solvent control and cisplatin 15.4 μM and rapamycin 50 nM were used as positive controls. The results are presented as mean ± SD of three independent assays. The symbol * indicates a p-value < 0.05.

Taken together our results show a simultaneous induction of apoptosis and autophagic cell death in cells exposed to complexes **1**–**3**, particularly when exposed to complex **3**. This may be due to the presence of the *terpy* ligand in all complexes but the planarity of **3** might provide an additional feature for increased internalization and cytotoxicity. In a recent work, terpyridine derived compounds were demonstrated to simultaneously induce apoptosis and autophagy in cancer cell lines exposed to them [102].

2.5.5. Intracellular reactive oxygen species (ROS) in HCT116 cell line exposed to complexes 1-3

Increased intracellular ROS have been correlated with the programmed cell death observed in cancer cell lines exposed to Au(III), Pt(II) and Cu(II) complexes bearing *terpy* ligands and were investigated in HCT116 exposed to IC_{50} concentrations of complexes **1**–**3** (Fig. 13) [97,98].

Exposure to complexes **1**–**3** induced an increase of 4.9 ×, 7.1 × and 11.4 ×, respectively, in intracellular ROS when compared with the DMSO control (Fig. 13). Complex **3**, bearing a Cu(II) centre, induces higher levels of intracellular of ROS than complexes **1** and **2**, which seems to be correlated with the higher levels of internalized Cu(II), the increased apoptosis and autophagy in HCT116 cells exposed to complex **3** (Figs. 9 and 12). It should be noted that despite mitochondria is the main site for ROS production within cells, we did not observe an increased mitochondria membrane destabilization with complex **3** meaning that the increase in ROS levels should be triggered by the complex. To validate this theory, HCT116 were pre-incubated for 1 h with N-acetyl-L-cysteine (NAC) a ROS scavenger [103]. Indeed, pre-incubation of cells with NAC, reduced the amount of ROS produced in HCT116 cell line by 21,7%, 45.8% and 63,5% in cells exposed to complex **1**, **2** and **3**, respectively (Fig. 13). Moreover, we further analysed if the trigger of apoptosis was due to ROS (Figure S22, ESI[1]). Pre-incubation with NAC reduced apoptosis in HCT116 exposed to complex **1**, **2** and **3** by 91%, 85% and 96% respectively (Figure S22). Taken together these results confirm previous observations in which ROS production is correlated with apoptosis and autophagic cell death induction in cancer cells exposed to metallic complexes bearing *terpy* ligands [97,98] and that complex **3** increased cytotoxicity is due to 1) increased internalization, 2) its ability to induce intracellular ROS that triggers autophagy and apoptosis.

2.5.6. Ex-ovo chorioallantoic membrane (CAM) in vivo assay

Ex-ovo chorioallantoic membrane (CAM) assay is a well-known *in vivo* model to assess cytotoxicity and also potential agents that can modulate angiogenesis [104]. To evaluate *in vivo* toxicity and pro-angiogenic or anti-angiogenic potential of complexes **1**–**3** was

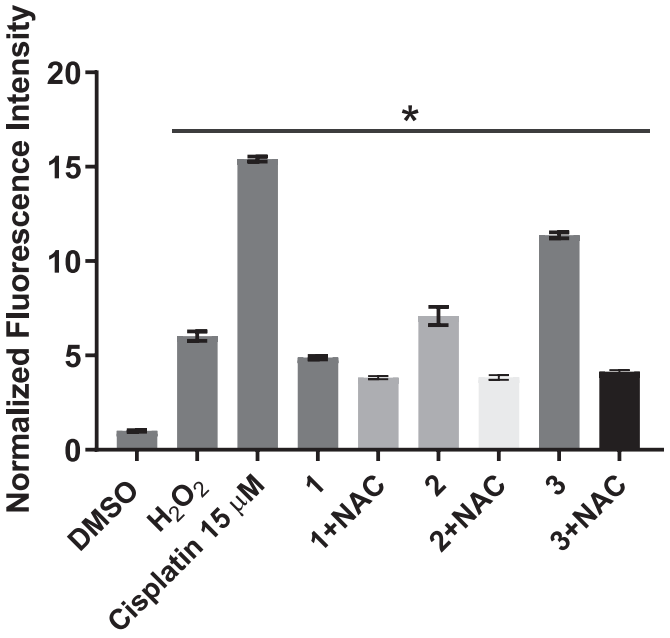

Fig. 13. Production of reactive oxygen species (ROS) in HCT116 cells exposed to IC_{50} concentrations of complexes **1**–**3** for 48 h evaluated by flow cytometry. DMSO 0.1% (v/v) was used as solvent control and cisplatin 15.4 μM and H_2O_2 50 μM were used as positive controls. HCT116 cells were also pre-incubated for 1 h at 37 °C with 5 mM of N-acetyl-cysteine (NAC) before incubation with complexes (indicated in the Figure with +NAC). The results are presented as mean ± SD of three independent assays. The symbol * indicates a p-value < 0.05.

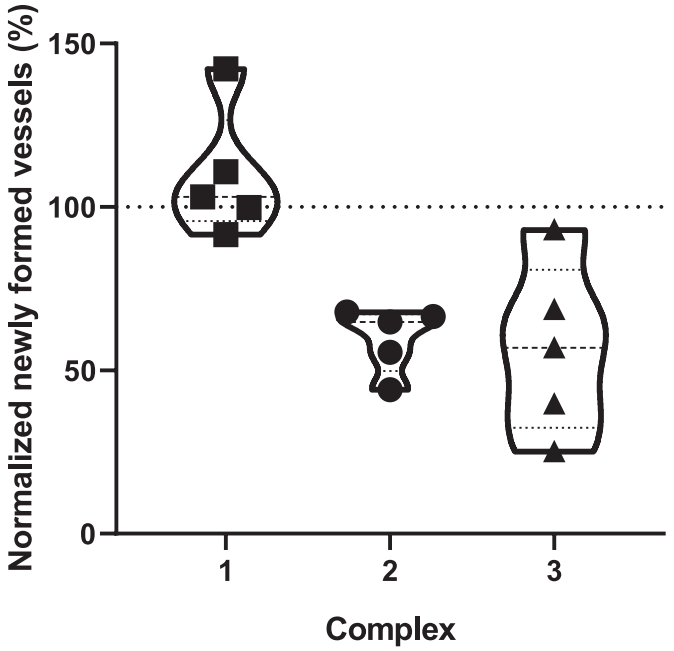

Fig. 14. Percentage of newly formed vessels in ex-ovo CAMs after 24 h exposure to IC_{50} concentrations of complexes **1**–**3**. At least 5 independent chicken embryos experiments were used to construct violin bars representing the distribution density and average of the normalized newly formed vessels. Normalization was performed using the percentage of tertiary veins obtained after exposure to DMSO 0.1% (v/v) to which the dotted line at 100% refers to. The results are presented as mean ± SD of five independent assays. The symbol * indicates a p-value <0.05.

measured by challenging CAMs of chicken embryos for 24 h with the IC_{50} concentrations of each complex and all newly formed vessels were counted at 0 h, 24 h and compared with the DMSO vehicle controls (Fig. 14).

Interestingly, no chicken embryos deaths were observed for the tested concentrations in all 5 independent CAM experiments, indicating that despite these concentrations can induce HCT116 loss of cell viability, they do not induce toxicity in this *in vivo* model.

What is more, complexes **2** and **3** show a high anti-angiogenic effect on the CAMs of chicken embryos, with a reduction of the average of newly formed vessels to 59.7% and 56.7%, respectively, when compared to DMSO control (Fig. 14), which might be highly interesting for their application in cancer context avoiding tumor angiogenesis, a process that is critical for tumor growth and metastization [105]. On the contrary, complex **1** seems to induce a slight increase of the average of newly formed vessels (Fig. 14). Pro-angiogenic and anti-angiogenic controls were also included in supplementary[1], Figure S23.

Taken together these results seem to indicate that complex **2** and **3** have an antiproliferative effect in colorectal cancer cells by inducing apoptosis (mostly **3**) and autophagy due to the generation of ROS and that there are able to inhibit the formation of newly blood vessels.

2.6. Conclusions

This work presents the synthesis, chemical and biological characterization of three complexes of Pt(II), Au(III), Cu(II) bound to *4′-(2-quin)-terpy* ligand.

All complexes displayed cytotoxic potential in A2780 and, mainly in HCT116 cancer cell lines following the order **3** > **2** > **1**. The complexes IC_{50} are at least 20 × lower than the IC_{50} displayed by cisplatin (15.4 μM) [100] in HCT116 cell line while displaying at the same time, much less cytotoxicity in normal dermal fibroblasts. Although the lower stability of complex **1** in PBS could explain the lower cytotoxicity of complex when compared to the others, the cytotoxic results seem to be correlated with the inclination angles of *2-quin* unit to the central pyridine. CD data seems to indicate that complex **3**, more planar, induces a high destabilization of the DNA double helix (shift from B-form to Z-form). Higher the deviation from planar, the lower the cytotoxicity displayed by the complexes. Cellular uptake may be also responsible for the cytotoxicity exhibited by complexes and while complex **2** seems to be passively internalized, complex **1** and **3** might enter cells via energy-dependent and -independent mechanisms. Complexes **1**–**3** were shown to induce ROS that might be associated with the increased apoptosis and autophagy. Moreover, all complexes dissipate the mitochondrial membrane potential leading to an increased BAX/BCL-2 ratio that triggered apoptosis. Complexes **2** and **3** were also shown to exhibit an anti-angiogenic effect by significantly reduce the number of newly formed blood vessel in a CAM model with no toxicity in this *in vivo* model.

Our results seem to suggest that the increased cytotoxicity of complex **3** and its potential interest for translation to pre-clinical mice xenografts might be associated with: 1) higher % of internalization of HCT116 cells via energy-dependent and -independent mechanisms; 2) its ability to intercalate DNA and due to its planarity induced higher destabilization of DNA (as measured *in vitro* by CD), that all together 3) induce intracellular ROS that trigger apoptosis and autophagy.

3. Experimental

3.1. Materials

The metal salts and solvents used for the synthesis were commercially available and were used without further purification.

All reagents and solvents used for the synthesis were of reagent grade, while the solvents for spectroscopic measurements were of HPLC grade. The ligand *4′-(2-quin)-terpy* was prepared according the modified method employed in our previous studies [106–108], and its purity was checked with ^{1}H NMR and elemental analysis (see Figure S5, ESI[1]).

3.2. Synthesis

3.2.1. Synthesis of [Pt(4′-(2-quin)-terpy)Cl](SO$_3$CF$_3$) (1)

[Pt(PhCN)$_2$Cl$_2$] (0.24 g, 0.5 mmol) dissolved in acetonitrile (30 ml) was added to a 10 ml solution of Ag(CF$_3$SO$_3$) (0.13 g, 0.5 mmol). The reaction mixture was heated under reflux for 12 h, after which the white precipitate of AgCl was removed by filtration. A solution of ligand *4′-(2-quin)-terpy* in acetonitrile (0.18 g, 0.5 mmol) was added to the filtrate. The resulted mixture was heated in a solvatothermal reactor under atmospheric pressure for 24 h and then gradually cooled for another 24 h. The X-ray quality orange crystals were obtained directly from mother liquor.

[Pt(4′-(2-quin)-terpy)Cl](SO$_3$CF$_3$) (1). Yield 65%. HRMS (ESI): calcd for $C_{24}H_{16}ClN_4Pt^+$ $[M]^+$ 590.0708 found 590.0710. **IR (cm^{-1}):** 439(w), 453(w), 475(w), 516(m), 572(m), 637(s), 663(w), 696(s), 700(s), 714(w), 748(m), 768(m), 784(s), 829(m), 869(w), 908(w), 1031(s), 1050(w), 1140(s), 1163(s), 1224(s), 1264(s), 1275(s), 1333(w), 1374(w), 1416(m), 1433(m), 1476(m), 1505(m), 1555(m), 1594(m), 1610(s), 2926(w), 3026(m), 3084(w), 3462(w). **UV–Vis (CH$_3$CN 5 × 10^{-5} M/nm, (ε × 10^3/M^{-1} × cm^{-1}):** 406 (8.52), 389 (7.11), 353 (10.77), 332 (24.35), 313 (20.89), 283 (34.34), 264 (32.10). **^{1}H NMR (400 MHz, DMSO)** δ 9.16 (s, 2H, H^{B2}), 8.72 (d, J = 8.0 Hz, 2H, H^{A4}), 8.70–8.63 (m, 3H, H$^{A1,\ C2}$), 8.46 (d, J = 8.6 Hz, 1H, H^{C3}), 8.41 (dt, J = 7.8, 1.2 Hz, 2H, H^{A3}), 8.18 (d, J = 8.4 Hz, 1H, H^{C6}), 8.08 (d, J = 7.9 Hz, 1H, H^{C9}), 7.91 (t, J = 7.6 Hz, 1H, H^{C7}), 7.82 (t, J = 6.6 Hz, 2H, H^{A2}), 7.77 (t, J = 7.5 Hz, 1H, H^{C8}). **^{13}C NMR (100 MHz, DMSO)** δ 158.3 (C^{A5}), 155.0 (C^{B1}), 151.7 (C^{A1}), 151.3 (C^{B3}), 151.3 (C^{C1}), 147.8 (C^{C4}), 143.1 (C^{A3}), 138.7 (C^{C2}), 131.4 (C^{C7}), 130.0 (C^{C6}), 129.8 (C^{A2}), 129.0 (C^{C8}), 128.7 (C^{C5}), 128.6 (C^{C9}), 126.7 (C^{A4}), 122.2 (C^{B2}), 119.8 (C^{C3}).

3.2.2. Synthesis of [Au(4′-(2-quin)-terpy)Cl](PF$_6$)$_2$CH$_3$CN (2)

KAuCl$_4$ (0.19 g, 0.5 mmol) dissolved in methanol/water (1:4 v/v) (50 ml) was added to the methanolic solution of ligand *4′-(2-quin)-terpy* (0.18 g, 0.5 mmol) and refluxed for 2 h. After that, an aqueous solution of NH_4PF_6 (0.20 g, 1.2 mmol) was added, and the resulting mixture was heated for another 2 h. The solution was allowed to evaporate in a hood at room temperature, which gave an orange microcrystalline precipitate of **2**. The X-ray quality crystals were grown by recrystallization of the precipitate from acetonitrile.

[Au(4′-(2-quin)-terpy)Cl](PF$_6$)$_2$CH$_3$CN (2). Yield 45%. HRMS (ESI): calcd for $C_{24}H_{16}ClN_4Au^+$ $[M]^{2+}$ 592.0724 found 592.0726. **IR (cm^{-1}):** 559(s), 688(w), 741(w), 783(m), 840(s), 1040(w), 1053(w), 1103(w), 1172(w), 1250(w), 1266(w), 1317(w), 1339(w), 1364(w), 1418(m), 1438(m), 1488(m), 1508(w), 1557(m), 1568(m), 1604(s), 3074(w), 3445(w). **UV–Vis (CH$_3$CN 5 × 10^{-5} M/nm, (ε × 10^3/M^{-1} × cm^{-1}):** 374 (21.00), 362 (23.09), 297 (21.87), 288 (22.03), 275 (22.69), 239 (43.88), 227 (52.84). **^{1}H NMR** (400 MHz, CD$_3$CN) δ 9.41 (s, 1H, H^{B2}), 9.20 (dd, J = 6.0, 1.2 Hz, 1H, H^{A1}), 8.82 (dd, 1H, H^{A4}), 8.75 (dt, J = 7.9, 1.3 Hz, 1H, H^{A3}), 8.71 (d, J = 8.7 Hz, 1H, H^{C2}), 8.48 (d, J = 8.6 Hz, 1H, H^{C3}), 8.34 (d, J = 8.5 Hz, 1H, H^{C6}), 8.17–8.10 (m, 2H, H$^{A2,\ C9}$), 7.99 (t, J = 7.7 Hz 1H, H^{C7}), 7.83 (t, J = 7.6 Hz 1H, H^{C8}). **^{13}C NMR** (100 MHz, CD$_3$CN) δ 159.6 (C^{A5}), 158.3 (C^{B3}), 153.9 (C^{B1}), 153.5 (C^{A1}), 150.4 (C^{C1}), 149.1 (C^{C5}), 148.2 (C^{A3}), 139.7 (C^{C2}), 132.5 (C^{C7}), 132.4 (C^{A2}), 131.1 (C^{C6}), 130.6 (C^{C8}), 130.4 (C^{A4}), 130.1 (C^{C4}), 129.1 (C^{C9}), 126.0 (C^{B2}), 120.4 (C^{C3}).

3.2.3. Synthesis of [Cu(4′-(2-quin)-terpy)Cl](PF$_6$) (3)

A solution of ligand *4′-(2-quin)-terpy* (0.04 g, 0.1 mmol) in CH_2Cl_2/CH_3OH (1:1 v/v) was poured into a glass test tube and a neat mixture of CH_2Cl_2/CH_3OH was carefully layered on the ligand solution. Then, the methanolic solution of $CuCl_2 \cdot 2H_2O$ (0.1 mmol, 0.02 g) mixed with NH_4PF_6 (0.25 mmol, 0.04 g) was layered on the above mixture. The test tube was sealed and the solutions were allowed to diffuse slowly. After about two weeks, needle-like green X-ray quality crystals of **3** were obtained.

[Cu(4′-(2-quin)-terpy)Cl](PF$_6$) (3). Yield 12%. HRMS (ESI): calcd for $C_{24}H_{16}ClN_4Cu^+$ $[M - Cl]^+$ 458.0354 found 458.0358. **IR (cm^{-1}):** 414(w), 483(w), 557(s), 657(w), 690(w), 738(w), 781(m), 840(s), 928(w), 1021(m), 1038(w), 1099(w), 1147(w), 1165(w), 1251(w), 1262(w), 1307(w), 1338(w), 1380(w), 1418(m), 1438(m), 1478(m), 1506(w), 1553(m), 1566(m), 1606(s), 1620(s), 3068(w), 3106(w), 3437(m). **UV–Vis (CH$_3$CN 5 × 10^{-5} M/nm, (ε × 10^3/M^{-1} × cm^{-1}):** 697 (1.30), 329 (26.57), 291 (33.88), 279 (37.27), 270 (37.57), 228 (53.35).

3.3. Instrumentation

The IR spectra were recorded on a Nicolet iS5 spectrophotometer in the range 4000–400 cm^{-1} using the KBr pellets technique. High resolution mass spectrometry analyses were performed on a Waters Xevo G2 Q-TOF mass spectrometer (Waters Corporation) equipped with an ESI source operating in positive-ion modes. Full-scan MS data were collected from 100 to 1000 Da in positive ion mode with scan time of 0.5 s. To ensure accurate mass measurements, data were collected in centroid mode and mass was corrected during acquisition using leucine enkephalin solution as an external reference (Lock-Spray™), which generated reference ion at *m/z* 556.2771 Da ($[M+H]^+$) in positive ESI mode. The accurate mass and composition for the molecular ion adducts were calculated using the MassLynx software (Waters) incorporated with the instrument. The NMR spectra were recorded using Bruker Avance 400 MHz spectrometer in dimethyl sulfoxide-d^6 ((CD$_3$)$_2$SO) for **1** and in acetonitrile-d^3 (CD$_3$CN) for **2**. Chemical shifts (δ) are reported in parts per million (ppm) and referenced to residual solvent peak ((CD$_3$)$_2$SO: ^{1}H δ = 2.50 ppm, ^{13}C δ = 39.52 ppm, CD$_3$CN: ^{1}H δ = 1.94 ppm, ^{13}C δ = 118.26 ppm). Coupling constants (J) are reported in Hz. The peak multiplicity is designated by a singlet (s), doublet (d), triplet (t), doublet of triplets (dt), and multiplet (m). Homonuclear correlation spectroscopy was performed using 2D COSY experiments, while heteronuclear correlation spectroscopy was done on the basis of HMQC or HMBC (long-range) experiments.

3.4. X-ray crystallography

The crystallographic data and refinement details are given in Table 3. The X-ray diffraction data was collected by means of Oxford Diffraction four-circle diffractometer Gemini A Ultra equipped with Atlas CCD detector and using graphite monochromated MoKα radiation (λ = 0.71073 Å) at room temperature. Diffraction data collection, cell refinement and data reduction were performed using CrysAlisPro software [109]. The structures were solved with SHELXS-2014 and refined with SHELXL-2014 [110,111], using full-matrix least-squares on F2. The non-hydrogen atoms were refined anisotropically while hydrogen atoms were placed in calculated positions and refined using idealized geometries (riding model) with fixed isotropic displacement parameters (for aromatic rings: Uiso(H) = 1.2 Ueq(C), d(C–H) = 0.93 Å; for methyl: Uiso(H) = 1.5 Ueq(C), d(C–H) = 0.96 Å). The methyl group was allowed to rotate around its local threefold axis. CCDC 1824952, 2053808, and 2053807 contain the crystallographic data for **1**–**3** and can be obtained free of charge from The Cambridge Crystallographic Data Centre at www.ccdc.cam.ac.uk/getstructures. Powder X-ray diffraction (PXRD) measurements were performed on a

Table 3
Crystal data and structure refinement.

Name	1	2	3
Empirical formula	$C_{25}H_{16}ClN_4PtF_3O_3S$	$C_{26}H_{19}AuClN_5F_{12}P_2$	$C_{24}H_{16}ClCuN_4F_6P$
Formula weight	740.02	923.82	604.37
Temperature [K]	295.0(2)	295.0(2)	295.0(2)
Wavelength [Å]	0.71073	0.71073	0.71073
Crystal system	Monoclinic	Monoclinic	Orthorhombic
Space group	$P2_1/n$	$P2_1/n$	*P*nma
Unit cell dimensions [Å,°]	$a = 7.02890(18)$ $b = 16.7405(4)$ $c = 20.3049(7)$ $\alpha = 90$ $\beta = 95.322(3)$ $\gamma = 90$	$a = 7.9118(2)$ $b = 29.5090(1)$ $c = 13.0714(3)$ $\alpha = 90$ $\beta = 95.179(3)$ $\gamma = 90$	$a = 15.3579(8)$ $b = 6.6271(4)$ $c = 22.7715(16)$ $\alpha = 90$ $\beta = 90$ $\gamma = 90$
Volume [$Å^3$]	2378.92(12)	3039.31(11)	2317.7(2)
Z	4	4	4
Density (calculated) [Mg/m^3]	2.066	2.019	1.732
Absorption coefficient [mm^{-1}]	6.160	5.136	1.198
F(000)	1424	1776	1212
Crystal size [mm]	0.07 × 0.11 × 0.23	0.03 × 0.19 × 0.25	0.06 × 0.07 × 0.57
θ range for data collection [°]	3.4 to 25.24	3.4 to 25.05	3.5 to 25.05
Index ranges	$-8 \le h \le 9$ $-23 \le k \le 21$ $-23 \le l \le 28$	$-9 \le h \le 8$ $-27 \le k \le 35$ $-15 \le l \le 15$	$-17 \le h \le 18$ $-7 \le k \le 7$ $-24 \le l \le 27$
Reflections collected	16071	16007	9293
Independent reflections	5695	5380	2242
Completeness to 2theta	99.7	99.7	99.6
Min. and max. transm.	0.5168 and 1.0000	0.3015 and 1.0000	0.7581 and 1.0000
Data/restraints/parameters	5695/0/343	5380/0/425	2242/0/217
Goodness-of-fit on F^2	1.065	1.073	1.032
Final R indices [$I > 2\sigma(I)$]	0.0313 (wR = 0.0578)	0.0434 (wR = 0.0977)	0.0524 (wR = 0.1321)
R indices (all data)	0.0496 (wR = 0.0660)	0.0558 (wR = 0.1030)	0.0720 (wR = 0.1400)
Largest diff. peak and hole [e $Å^{-3}$]	0.635 and −0.871	1.410 and −1.370	0.803 and −0.442
CCDC number	1824952	2053808	2053807

PANalytical Empyrean X-ray diffractometer with Cu−K_α radiation (λ = 1.5418 Å), in which the X-ray tube was operated at 40 kV and 30 mA ranging from 5 to 40°. The experimental diffraction pattern was compared with the theoretical one generated using single crystal X-ray data (Figure S24, ESI[1]).

3.5. Spectroscopy and stability

The UV−Vis spectra were obtained using Nicolet Evolution 220 in acetonitrile, DMSO and Dulbecco's Modified Phosphate Buffered Saline (PBS, pH 7.4, 130 mM NaCl, Sigma Aldrich) solutions in the range 220−1000 nm. The stability of the compounds in solution of acetonitrile, DMSO and PBS was checked by measuring the spectra of the sample (50 μM) once every 4 h for 48 h at room temperature. Stability of **1**−**3** in the presence of biologically important reducing agents was tested by means of the UV−Vis monitoring. PBS mixtures of the tested complex (50 μM) with reduced glutathione (50 μM or 1 mM) or sodium ascorbate (50 μM) were measured every 20 min for 6 h at room temperature.

3.6. DNA-binding

The experiments were carried out in PBS at room temperature. The concentration of calf thymus DNA (CT-DNA, Sigma Aldrich) was determined by measurement of UV−Vis absorbance at 260 nm (A_{260}), using Beer-Lambert law with ε_{260} = 6600 M^{-1} cm^{-1} as the CT-DNA molar absorption coefficient [112]. The ratio A_{260}/A_{280} of the solution was in the range 1.85−1.90, indicating that the CT-DNA was sufficiently free of protein [113]. Stock solution of CT-DNA was stored at 4 °C and used in less than 4 days. Concentrated stock solutions of metal complexes were prepared by dissolving the complex in 0.1 ml of DMSO and diluted with PBS to suitable concentrations for all the experiments.

3.6.1. UV−vis spectrophotometric DNA titration

The electronic absorption titrations of complexes with CT-DNA were carried out on ThermoScientific NanoDrop OneC UV−Vis spectrophotometer with use of l = 1 cm cuvette holder in 37 °C. The complexes were dissolved in PBS in constant concentrations (5 μM for **1** and 25 μM for **2** and **3**) and were titrated with increasing concentrations of CT-DNA for various r ([DNA]/[complex]) ratios until full binding was achieved. After each addition of CT-DNA, the mixture was magnetically stirred and incubated for 8 min before the spectra were recorded. The equal amounts of CT-DNA were added to both the complex and the reference solutions to eliminate the absorbance of CT-DNA itself. The obtained data was analysed using Benesi-Hildebrand equation (2) [114−116]:

$$\frac{A_0}{A - A_0} = \frac{\varepsilon_G}{\varepsilon_{H-G}} + \frac{\varepsilon_G}{\varepsilon_{H-G}} \times \frac{1}{K_b\,[DNA]} \quad (2)$$

where A and A_0 are the absorbances of the complex with and without DNA, respectively, and ε_G and $\varepsilon_{H\text{-}G}$ are molar extinction coefficients of the complex in its free and bound forms. The binding constants K_b were calculated from linear plots of $A_0/(A-A_0)$ vs 1/[DNA] by the ratio of intercept to the slope (Figure S18).

3.6.2. Ethidium bromide displacement assay

Fluorescence quenching experiments were carried out on Edinburgh FLS-980 spectrophotometer using ethidium bromide (EB, Sigma Aldrich) fluorescence displacement assay. Equimolar amount of EB and CT-DNA solutions were mixed at room temperature and incubated for 2 h in the dark. The tested complex was then titrated into the formed EB−CT-DNA adduct and incubated for additional 30 min. The final concentration of the EB−CT-DNA adduct was 50 μM and the concentration of the complexes varied from 0 to 50 μM. Fluorescence spectra of the samples were obtained

at excitation wavelength 510 nm and emission 618 nm. The quenching data was further analysed according to the linear Stern-Volmer equation (3), which was used to calculation of the binding constant K_{app} (4):

$$I_0 / I = 1 + K_{SV}[Q] \quad (3)$$

$$K_{app}\left[Q_{1/2}\right] = K_{EB}[EB] \quad (4)$$

where I_0 and I are the fluorescence intensity in the absence and presence of the complexes; K_{SV} is the Stern-Volmer quenching constant; [Q] is the concentration of the complexes; $[Q_{1/2}]$ is the concentration of the complex causing 50% reduction in the fluorescence intensity; $K_{EB} = 1 \times 10^7\ M^{-1}$; [EB] = 5×10^{-5} M.

3.6.3. Circular dichroism

Circular dichroism spectra were performed after incubation of 12.5 μM calf thymus DNA (CT-DNA, Thermo Fisher Scientific) with 0, 12.5 and 25 μM of complex **1**, **2** or **3**. As solvent controls, 12.5 μM calf thymus DNA was incubated with 0, 2.5 and 5% DMSO. All samples were incubated in 5 mM tris-HCl pH 7.0 with 50 mM NaCl, for 6 h at 37 °C. The screening of each sample was performed in triplicate in a Chirascan qCD from AppliedPhotophysics (Surrey, United Kingdom) using a 1 cm (1 mL) quartz cuvette, ranging from 230 to 600 nm. CD spectra were performed at BIOLAB (UCIBIO, Caparica). The CD spectra of the complexes were also acquired after incubation of 25 μM of complex **1**, **2** or **3**, and DMSO 5% (vehicle control) in 5 mM tris-HCl pH 7.0 with 50 mM NaCl, for 6 h at 37 °C.

3.7. Biological studies

3.7.1. Cell culture

A2780 (Merck, Darmstadt, Germany) and HCT116 cancer cell lines and normal dermal fibroblasts (American Type Culture Collection, ATCC, Manassas, VA, USA), were maintained as previously described [117,118]. RPMI 1640 medium was used to cultivated A2780 cell lines and DMEM, Dulbecco's Modified Eagle medium, was used to cultivate HCT116 cells and fibroblasts. Media were supplemented with 10% (v/v) fetal bovine serum, FBS, and with PenStrep solution 1% (v/v) (all media and supplements from Thermo Fischer Scientific, Waltham, MA, USA). Cells were incubated in a humidified atmosphere with 5% CO_2 (v/v) at 37 °C, at all times.

3.7.2. Viability assays

Cells were cultivated in 96-well plates at a density of 7.5×10^5 cells/ml and incubated for 24 h prior to incubation with several concentrations of complexes **1**–**3** dissolved in culture media. DMSO 0.1% (solvent control) and cisplatin (positive control) were used as internal controls in all replicates. Cell cultures were incubated for 48 h before the CellTiter 96® Aqueous Non-Radioactive Proliferation assay (Promega, Madison, WI, USA) was used to determine the cellular viability (MTS assay) [117]. The Tecan microplate reader, Infinite M200 (Tecan, Männedorf, Switzerland) was used to read absorbance at 490 nm and the analyses of dose response curves and the determination of the half maximal inhibitory concentration (IC_{50}) was performed with the GraphPad Prism 8.2.1 software (GraphPad Software, La Jolla, CA, USA).

3.7.3. ICP-AES

Cellular uptake of these complexes **1**–**3** was determined by inductively coupled plasma atomic emission spectrometry (ICP-AES) was used to determine the amount of molecular Pt, Au and Cu that remained in the supernatant after exposure of HCT116 cells for 4 h to IC_{50} concentrations of complexes **1**–**3** incubated at 4 °C and 37 °C. HCT116 cells were seeded into 25 cm^2 T-flasks (5×10^6 cells per flask) and incubated for 24 h at 37 °C. Then fresh culture media was added with IC_{50} concentrations of the complexes, and cells were further incubated for 4 h at 4 °C or 37 °C. DMSO 0.1% (v/v) was used as vehicle control. After 4 h incubation, the supernatant was recovered and fresh *acqua regia* (3:1 HCl:HNO_3) was added to supernatants and cells were incubated o.n. in a hood at RT. HCT116 cells without any treatment were used to provide biological matrix to perform Pt, Au and Cu standards. ICP-AES was performed as a paid service in Laboratório de Análises/LAQV.

3.7.4. Analysis of apoptosis induction in HCT116 cell line evaluated with the annexin V-Alexa fluor 488/PI double staining assay

As previously described, HCT116 cells were seeded in 6-well plates at a density of 1×10^5 cells/ml, incubated for 24 h and then incubated for another 48 h with IC_{50} concentrations of complexes **1**–**3** dissolved in DMEM media [117,119]. HCT116 cells samples were also pre-treated with 5 mM N-acetyl cysteine (NAC) before removal of culture media and incubation with the complexes. Cells treated with DMSO 0.1% and cisplatin 15.4 μM were used as vehicle and positive controls, respectively. After 48 h incubation, cells were washed with PBS 1X, treated with Tryple Express (ThermoFisher Scientific), washed again with PBS 1X and incubated for 15 min at room temperature with 10 μg/ml propidium iodide and Annexin V-Alexa fluor 488 assay solution. Cells were then processed in an Attune acoustic focusing flow cytometer and the respective Attune Cytometric Software 2.1 (ThermoFisher Scientific) was used to collect and analyze experimental results.

3.7.5. Western blot for apoptotic index determination

The western-blot analysis for BAX and BCL-2 protein expression quantification followed the same procedure described before ([120] with few modifications. Briefly, 4×10^6 HCT116 cells were incubated in 25 cm^2 T-flasks for 24 h. Afterwards, the medium was replaced by fresh medium supplemented with 0.1% (v/v) DMSO, or the IC_{50} of complex **1**, **2** or **3**. After 48 h, cell monolayer was washed three times with PBS, scraped from the surface with PBS and centrifuged at 500×*g* for 5 min. Whole protein extract was obtained as described before [121]. The membrane was incubated for 1 h with fresh 5% non-fat milk in 1X TBST buffer (50 mM Tris, 150 mM NaCl and 0.1% (v/v) Tween 20, pH ~7.5) to block non-specific protein bidding. Then, each nitrocellulose membrane was exposed to different primary antibody in 5% non-fat milk in TBST, namely *anti*-Bax (1:5000; Abcam, United Kingdom) and anti Bcl-2 (1:1000; Sigma, St. Louis, EUA) and was left to incubate for 1 h at RT, with constant agitation. Concluded this incubation, the membrane was washed three times with 1X TBST buffer with agitation for 5 min at RT. The same procedure above was also employed to the membrane incubation with the secondary antibody (1:3000, Anti-mouse IgG, horseradish peroxidase (HPR)-linked Antibody or 1:2000, Anti-rabbit IgG, HPR-linked Antibody; Cell Signalling Technology, USA). All membranes were stripped with stripping buffer (0.1 M glycine, 20 mM magnesium acetate and 50 mM potassium chloride) and, then, re-incubated with *anti*-β actin (1:5000; Sigma, St. Louis, EUA) as a control for further normalization of the results. To detect the protein bands, a WesternBright ECL subtract (Advansta, USA) was prepared and membranes incubated for 5 min. Sequentially, the film was exposed to the membrane, on a dark room. The quantification of proteins was determinate by densitometry using Image J software. The BAX and BCL-2 protein band intensities were normalized to the intensities of the total protein of the respective band after staining of the membrane with Ponceau S stain (Pierce) and then to the values of DMSO treated samples.

3.7.6. Evaluation of mitochondrial membrane potential ($\Delta\Psi M$) changes due to exposure to complexes 1-3

As described elsewhere, HCT116 cells were plated at 7.5×10^5 cells per ml in 6-well plates, incubated for 24 h. Fresh medium was then added containing IC_{50} concentrations of complexes **1**–**3**. Cells exposed DMSO 0.1% (solvent control) and cisplatin 15.4 μM were also used as controls. After 48 h incubation, cells were washed with PBS 1X, treated with Tryple Express and washed again with PBS 1X prior to incubation with JC-1 dye, 5,5′,6,6′-tetrachloro-1,1′,3,3′-tetraethylbenzimidazolylcarbocyanine iodide (JC-1, Abnova Corporation, Walnut, CA, USA) following the recommendations of the manufacturer (20 min at 37 °C) [122]. The fluorescence of cells was then measured by flow cytometry using an Attune acoustic focusing flow cytometer (ThermoFisher Scientific) in the BL-1 ("green") and BL-2 ("red") filters and data was collected with the respective software. Fluorescence ratios were normalized to the DMSO control.

3.7.7. Analysis of autophagy induction in HCT116 cell line evaluated with the autophagy assay

HCT116 cells were cultivated in 6-well plates at a density of 1×10^5 cells/ml and incubated for 24 h prior to exposure to IC_{50} concentrations of complexes **1**–**3**. DMSO 0.1% was used as solvent control and cisplatin 15.4 μM and rapamycin 50 nM were used as positive controls. After 48 h incubation, HCT116 cells were washed with PBS 1X, treated with Tryple express and washed again with PBS 1X before the Autophagy Assay Kit (Abcam, Cambridge, UK) was used according to the manufacturer's instructions. The kit uses a cationic amphiphilic tracer dye that specifically labels pre-autophagosomes, autophagosomes and autolysosomes that are present in cells undergoing autophagy [100]. After staining cells were screened in an Attune acoustic focusing flow cytometer and the experiment information was treated with the respective Attune Cytometric Software 2.1 (ThermoFisher Scientific).

3.7.8. Production of reactive oxygen species (ROS) in HCT116 cell line exposed to complexes 1-3

HCT116 cells were seeded in 6-well plates at a density of 1×10^5 cells/ml and incubated initially for 24 h, before another 48 h incubation with IC_{50} concentrations of complexes **1**–**3**. Cell samples were pre-treated with 5 mM N-acetyl cysteine (NAC) before removal of culture media and incubation with the complexes. As controls, cells treated with DMSO 0.1% (vehicle control), cisplatin 15.4 μM and H_2O_2 50 μM (positive controls) were also used. Cells were washed with PBS 1X before treatment with Tryple express and washed twice with PBS 1X before incubation with of 2,7-dichlorodihydrofluorescein diacetate (H_2DCF-DA) 10 μM. Cells were then incubated for 30 min at 37 °C before being analysed in an Attune acoustic focusing cytometer and respective software (ThermoFisher Scientific) according to previously described protocols [100,117]. The ROS induced removal of acetate groups from H_2DCF-DA by intracellular esterases will turn this compound fluorescent and identify ROS production within HCT116 cells.

3.7.9. Toxicity and anti- or pro-angiogenic potential of complexes of 1–3 determined by ex-ovo CAM assays

As described previously the ex-ovo chorioallantoic membrane (CAM) assay was performed to evaluate the effect of complexes **1**–**3** on the formation of novel blood vessels in the chicken embryo [122,123]. Briefly, of chicken embryos in weighing boats were incubated for 24 h (embryo stabilization) before IC_{50} concentrations of complexes **1**–**3**, dissolved in PBS, were placed in the centre of O-rings and were incubated for 24 h at 37 °C. Images were taken at time point 0 h and 24 h and newly formed blood vessels (tertiary veins) were counted as described in the literature [120,122]. For control purposes it was also included DMSO 0.1% in PBS and anti-angiogenic and pro-angiogenic peptides [122]. The o-ring distribution in the chick embryos was assigned to ensure that each embryo was challenged with DMSO 0.1% and to prevent duplication of the same complex distribution scheme in different chicken embryos tested. This ex-ovo assay complies with the "3Rs policy" for animal experiment and is in accordance with Directive 2010/63/EU of the European Parliament for the protection of animal models for scientific purposes.

3.8. Statistical analysis

All results are presented as Mean ± SD from at least three independent experiments unless otherwise stated. One or two-way ANOVA or Student's t-test were used to determine statistical significance ($p < 0.05$) using the GraphPad Prism 8.2.1 software (GraphPad Software, San Diego, CA, USA).

Declaration of competing interest

The authors declare that they have no known competing financial interests or personal relationships that could have appeared to influence the work reported in this paper.

Acknowledgments

This work was supported by the Applied Molecular Biosciences Unit - UCIBIO which is financed by national funds from FCT (UIDP/04378/2020, UIDB/04378/2020 and fellowships SFRH/BPD/124612/2016 (C. Roma-Rodrigues), and PTDC/CVT-EPI/6685/2014 (L R. Raposo)).

Appendix A. Supplementary data

Supplementary data to this article can be found online at https://doi.org/10.1016/j.ejmech.2021.113404.

References

[1] R.A. Alderden, M.D. Hall, T.W. Hambley, The discovery and development of cisplatin, J. Chem. Educ. 83 (2006) 728, https://doi.org/10.1021/ed083p728.
[2] N.P.E. Barry, P.J. Sadler, Exploration of the medical periodic table: towards new targets, Chem. Commun. 49 (2013) 5106–5131, https://doi.org/10.1039/C3CC41143E.
[3] I. Ott, R. Gust, Non platinum metal complexes as anti-cancer drugs, Archiv Der Pharmazie 340 (2007) 117–126, https://doi.org/10.1002/ardp.200600151.
[4] U. Ndagi, N. Mhlongo, M.E. Soliman, Metal complexes in cancer therapy - an update from drug design perspective, Drug Des. Dev. Ther. 11 (2017) 599–616, https://doi.org/10.2147/DDDT.S119488.
[5] K.M. Deo, B.J. Pages, D.L. Ang, C.P. Gordon, J.R. Aldrich-Wright, Transition metal intercalators as anticancer agents—recent advances, Int. J. Mol. Sci. 17 (2016) 1818, https://doi.org/10.3390/ijms17111818.
[6] Y.-Y. Qi, Q. Gan, Y.-X. Liu, Y.-H. Xiong, Z.-W. Mao, X.-Y. Le, Two new Cu(II) dipeptide complexes based on 5-methyl-2-(2′-pyridyl)benzimidazole as potential antimicrobial and anticancer drugs: special exploration of their possible anticancer mechanism, Eur. J. Med. Chem. 154 (2018) 220–232, https://doi.org/10.1016/j.ejmech.2018.05.023.
[7] S. Perontsis, E. Geromichalou, F. Perdih, A.G. Hatzidimitriou, G.D. Geromichalos, I. Turel, G. Psomas, Synthesis, structural determination, in vitro and in silico biological evaluation of divalent or trivalent cobalt complexes with indomethacin, J. Inorg. Biochem. 212 (2020) 111213, https://doi.org/10.1016/j.jinorgbio.2020.111213.
[8] K.E. Erkkila, D.T. Odom, J.K. Barton, Recognition and reaction of metallointercalators with DNA, Chem. Rev. 99 (1999) 2777–2796, https://doi.org/10.1021/cr9804341.
[9] B.M. Zeglis, V.C. Pierre, J.K. Barton, Metallo-intercalators and metallo-insertors, Chem. Commun. (2007) 4565–4579, https://doi.org/10.1039/B710949K, 0.
[10] S.U. Rehman, T. Sarwar, M.A. Husain, H.M. Ishqi, M. Tabish, Studying non-covalent drug–DNA interactions, Arch. Biochem. Biophys. 576 (2015) 49–60, https://doi.org/10.1016/j.abb.2015.03.024.
[11] K. Suntharalingam, R. Vilar, Interaction of metal complexes with nucleic

acids, Annu. Rep. Prog. Chem., Sect. A: Inorg. Chem. 107 (2011) 339–358, https://doi.org/10.1039/C1IC90027G.
[12] B.J. Pages, D.L. Ang, E.P. Wright, J.R. Aldrich-Wright, Metal complex interactions with DNA, Dalton Trans. 44 (2015) 3505–3526, https://doi.org/10.1039/C4DT02700K.
[13] T.J.P. McGivern, S. Afsharpour, C.J. Marmion, Copper complexes as artificial DNA metallonucleases: from Sigman's reagent to next generation anticancer agent? Inorg. Chim. Acta. 472 (2018) 12–39, https://doi.org/10.1016/j.ica.2017.08.043.
[14] R. Galindo-Murillo, J.C. García-Ramos, L. Ruiz-Azuara, T.E. Cheatham, F. Cortés-Guzmán, Intercalation processes of copper complexes in DNA, Nucleic Acids Res. 43 (2015) 5364–5376, https://doi.org/10.1093/nar/gkv467.
[15] U. Jungwirth, C.R. Kowol, B.K. Keppler, C.G. Hartinger, W. Berger, P. Heffeter, Anticancer activity of metal complexes: involvement of redox processes, Antioxidants Redox Signal. 15 (2011) 1085–1127, https://doi.org/10.1089/ars.2010.3663.
[16] V. Uma, M. Elango, B.U. Nair, Copper(II) terpyridine complexes: effect of substituent on DNA binding and nuclease activity, Eur. J. Inorg. Chem. (2007) 3484–3490, https://doi.org/10.1002/ejic.200700053, 2007.
[17] I. Eryazici, C.N. Moorefield, G.R. Newkome, Square-planar Pd(II), Pt(II), and Au(III) terpyridine complexes: their syntheses, physical properties, supramolecular constructs, and biomedical activities, Chem. Rev. 108 (2008) 1834–1895, https://doi.org/10.1021/cr0781059.
[18] I. Ott, On the medicinal chemistry of gold complexes as anticancer drugs, Coord. Chem. Rev. 253 (2009) 1670–1681, https://doi.org/10.1016/j.ccr.2009.02.019.
[19] V. Singh, K. Sharma, B. Shankar, S.K. Awasthi, R.D. Gupta, Heteroleptic Cu(II)–polypyridyl complexes as photonucleases, New J. Chem. 40 (2016) 5906–5913, https://doi.org/10.1039/C6NJ00409A.
[20] P. Shi, M. Lin, J. Zhu, Y. Zhang, Q. Jiang, DNA-binding affinity and nuclease activity of two cytotoxic copper terpyridine complexes, J. Biochem. Mol. Toxicol. 23 (2009) 295–302, https://doi.org/10.1002/jbt.20292.
[21] B.Đ. Glišić, J. Nikodinovic-Runic, T. Ilic-Tomic, H. Wadepohl, A. Veselinović, I.M. Opsenica, M.I. Djuran, Synthesis, cytotoxic activity and DNA-binding properties of copper(II) complexes with terpyridine, Polyhedron 139 (2018) 313–322, https://doi.org/10.1016/j.poly.2017.11.008.
[22] V.M. Manikandamathavan, M. Thangaraj, T. Weyhermuller, R.P. Parameswari, V. Punitha, N.N. Murthy, B.U. Nair, Novel mononuclear Cu (II) terpyridine complexes: impact of fused ring thiophene and thiazole head groups towards DNA/BSA interaction, cleavage and antiproliferative activity on HepG2 and triple negative CAL-51 cell line, Eur. J. Med. Chem. 135 (2017) 434–446, https://doi.org/10.1016/j.ejmech.2017.04.030.
[23] D. Mahendiran, R.S. Kumar, A.K. Rahiman, Heteroleptic silver(I) complexes with 2,2′:6′,2″-terpyridines and naproxen: DNA interaction, EGFR/VEGFR2 kinase, growth inhibition and cell cycle arrest studies, Mater. Sci. Eng. C 76 (2017) 601–615, https://doi.org/10.1016/j.msec.2017.03.085.
[24] B. Deka, T. Sarkar, S. Banerjee, A. Kumar, S. Mukherjee, S. Deka, K.K. Saikia, A. Hussain, Novel mitochondria targeted copper(II) complexes of ferrocenyl terpyridine and anticancer active 8-hydroxyquinolines showing remarkable cytotoxicity, DNA and protein binding affinity, Dalton Trans. 46 (2017) 396–409, https://doi.org/10.1039/C6DT03660K.
[25] H.-H. Zou, L. Wang, Z.-X. Long, Q.-P. Qin, Z.-K. Song, T. Xie, S.-H. Zhang, Y.-C. Liu, B. Lin, Z.-F. Chen, Preparation of 4-([2,2′:6′,2″-terpyridin]-4′-yl)-N,N-diethylaniline NiII and PtII complexes and exploration of their in vitro cytotoxic activities, Eur. J. Med. Chem. 108 (2016) 1–12, https://doi.org/10.1016/j.ejmech.2015.11.005.
[26] J. Grau, R.F. Brissos, J. Salinas-Uber, A.B. Caballero, A. Caubet, O. Roubeau, L. Korrodi-Gregório, R. Pérez-Tomás, P. Gamez, The effect of potential supramolecular-bond promoters on the DNA-interacting abilities of copper–terpyridine compounds, Dalton Trans. 44 (2015) 16061–16072, https://doi.org/10.1039/C5DT02211H.
[27] S. Wang, W. Chu, Y. Wang, S. Liu, J. Zhang, S. Li, H. Wei, G. Zhou, X. Qin, Synthesis, characterization and cytotoxicity of Pt(II), Pd(II), Cu(II) and Zn(II) complexes with 4'-substituted terpyridine, Appl. Organomet. Chem. 27 (2013) 373–379, https://doi.org/10.1002/aoc.2988.
[28] W. Chu, Y. Wang, S. Liu, X. Yang, S. Wang, S. Li, G. Zhou, X. Qin, C. Zhou, J. Zhang, Synthesis, cytotoxicity and DNA-binding properties of Pd(II), Cu(II) and Zn(II) complexes with 4′-(4-(2-(piperidin-1-yl)ethoxy)phenyl)-2,2′:6′,2″-terpyridine, Bioorg. Med. Chem. Lett 23 (2013) 5187–5191, https://doi.org/10.1016/j.bmcl.2013.07.003.
[29] G. Annibale, M. Brandolisio, B. Pitteri, New routes for the synthesis of chloro(diethylenetriamine) platinum(II) chloride and chloro(2,2′ : 6′,2″-terpyridine) platinum(II) chloride dihydrate, Polyhedron 14 (1995) 451–453, https://doi.org/10.1016/0277-5387(94)00408-7.
[30] R. Büchner, J.S. Field, R.J. Haines, C.T. Cunningham, D.R. McMillin, Luminescence properties of salts of the [Pt(trpy)Cl]+ and [Pt(trpy)(MeCN)]2+ Chromophores: crystal structure of [Pt(trpy)(MeCN)](SbF6)2, Inorg. Chem. 36 (1997) 3952–3956, https://doi.org/10.1021/ic961068b.
[31] R. Büchner, C.T. Cunningham, J.S. Field, R.J. Haines, D.R. McMillin, G.C. Summerton, Luminescence properties of salts of the [Pt(4′Ph-terpy)Cl]+ chromophore: crystal structure of the red form of [Pt(4′Ph-terpy)Cl]BF4 (4′Ph-terpy = 4′-phenyl-2,2′:6′,2″-terpyridine), J. Chem. Soc., Dalton Trans. (1999) 711–718, https://doi.org/10.1039/A807914E, 0.
[32] J. Huo, N. Arulsamy, J.O. Hoberg, Facile synthesis and platinum complexes of 4′,5,5″-trisubstituted-2,2′:6′,2″-terpyridines, Dalton Trans. 40 (2011) 7534–7540, https://doi.org/10.1039/C1DT10465A.
[33] G.A. Lawrance, Coordinated trifluoromethanesulfonate and fluorosulfate, Chem. Rev. 86 (1986) 17–33, https://doi.org/10.1021/cr00071a002.
[34] A.M. Heyns, G.J. van Schalkwyk, A study of the infrared and Raman spectra of ammonium hexafluorophosphate NH4PF6 over a wide range of temperatures, Spectrochim. Acta Mol. Spectros 29 (1973) 1163–1175, https://doi.org/10.1016/0584-8539(73)80154-0.
[35] C.F. Macrae, I.J. Bruno, J.A. Chisholm, P.R. Edgington, P. McCabe, E. Pidcock, L. Rodriguez-Monge, R. Taylor, J. van de Streek, P.A. Wood, Mercury CSD 2.0 – new features for the visualization and investigation of crystal structures, J. Appl. Crystallogr. 41 (2008) 466–470, https://doi.org/10.1107/S0021889807067908.
[36] W. Fang, C. Liu, J. Chen, Z. Lu, Z.-M. Li, X. Bao, T. Tu, The electronic effects of ligands on metal-coordination geometry: a key role in the visual discrimination of dimethylaminopyridine and its application towards chemo-switch, Chem. Commun. 51 (2015) 4267–4270, https://doi.org/10.1039/C5CC00196J.
[37] J.E. Beves, E.C. Constable, S. Decurtins, E.L. Dunphy, C.E. Housecroft, T.D. Keene, M. Neuburger, S. Schaffner, J.A. Zampese, Structural diversity in the reactions of 4′-(pyridyl)-2,2′:6′,2″-terpyridine ligands and bis{4′-(4-pyridyl)-2,2′:6′,2″-terpyridine}iron(II) with copper(II) salts, CrystEngComm 11 (2009) 2406–2416, https://doi.org/10.1039/B909639F.
[38] E.J. Cho, S. Jung, K. Lee, H.J. Lee, K.C. Nam, H.-J. Bae, Fluorescent receptor-immobilized silica-coated magnetic nanoparticles as a general binding agent for histidine-tagged proteins, Chem. Commun. 46 (2010) 6557–6559, https://doi.org/10.1039/C0CC00991A.
[39] K. Suntharalingam, A.J.P. White, R. Vilar, Two metals are better than one: investigations on the interactions between dinuclear metal complexes and quadruplex DNA, Inorg. Chem. 49 (2010) 8371–8380, https://doi.org/10.1021/ic100884p.
[40] V.M. Manikandamathavan, V. Rajapandian, A.J. Freddy, T. Weyhermüller, V. Subramanian, B.U. Nair, Effect of coordinated ligands on antiproliferative activity and DNA cleavage property of three mononuclear Cu(II)-terpyridine complexes, Eur. J. Med. Chem. 57 (2012) 449–458, https://doi.org/10.1016/j.ejmech.2012.06.039.
[41] D. Xia, L. Liu, X. Ma, J. Ma, J. Yao, Crystal structure of dichloro(4'-(4-t-butylphenyl)- 2,2':6',2"-terpyridyl)copper(II), CuCl2(C25H23N3), Z. Kristallogr. N. Cryst. Struct. 227 (2014) 133–134, https://doi.org/10.1524/ncrs.2012.0061.
[42] T.-H. Huang, M.-H. Zhang, C.-Y. Gao, L.-T. Wang, Synthesis, structures and characterization of metal complexes containing 4′-phenyl-2,2′:6′,2″-terpyridine ligands with extended π···π interactions, Inorg. Chim. Acta. 408 (2013) 91–95, https://doi.org/10.1016/j.ica.2013.08.024.
[43] Z. Ma, L. Wei, E.C.B.A. Alegria, L.M.D.R.S. Martins, M.F.C.G. da Silva, A.J.L. Pombeiro, Synthesis and characterization of copper(II) 4′-phenyl-terpyridine compounds and catalytic application for aerobic oxidation of benzylic alcohols, Dalton Trans. 43 (2014) 4048–4058, https://doi.org/10.1039/C3DT53054J.
[44] S. Bhowmik, B.N. Ghosh, K. Rissanen, Transition metal ion induced hydrogelation by amino-terpyridine ligands, Org. Biomol. Chem. 12 (2014) 8836–8839, https://doi.org/10.1039/C4OB01867B.
[45] G. Zhang, E. Liu, C. Yang, L. Li, J.A. Golen, A.L. Rheingold, Copper(II) complexes of 2,2′:6′,2″-terpyridine derivatives for catalytic aerobic alcohol oxidations – observation of mixed-valence CuICuII assembles, Eur. J. Inorg. Chem. (2015) 939–947, https://doi.org/10.1002/ejic.201403140, 2015.
[46] K. Czerwińska, B. Machura, S. Kula, S. Krompiec, K. Erfurt, C. Roma-Rodrigues, A.R. Fernandes, L.S. Shul'pina, N.S. Ikonnikov, G.B. Shul'pin, Copper(II) complexes of functionalized 2,2′:6′,2″-terpyridines and 2,6-di(thiazol-2-yl)pyridine: structure, spectroscopy, cytotoxicity and catalytic activity, Dalton Trans. 46 (2017) 9591–9604, https://doi.org/10.1039/C7DT01244F.
[47] T. Rojo, M.I. Arriortua, J. Ruiz, J. Darriet, G. Villeneuve, D. Beltran-Porter, Magnetostructural correlations in parallel square-planar chloride bridged copper(II) dimers: structure, dynamic nuclear magnetic resonance study, and magnetic properties of [Cu2(terpy)2Cl2][PF6]2, J. Chem. Soc., Dalton Trans. (1987) 285–291, https://doi.org/10.1039/DT9870000285.
[48] J. Valdés-Martínez, D. Salazar-Mendoza, R.A. Toscano, Di-μ-chloro-bis-[(2,2′:6,2″-ter-pyridine)copper(II)] diperchlorate, Acta Crystallogr. 58 (2002) m712–m714, https://doi.org/10.1107/S1600536802020470.
[49] X.-H. Jin, L.-X. Cai, J.-K. Sun, Z.-F. Ju, J. Zhang, pH-induced coordination assembly of mononuclear and dinuclear copper(II) complexes based on a 4,4′-bipyridinium analogue, Inorg. Chem. Commun. 13 (2010) 86–89, https://doi.org/10.1016/j.inoche.2009.10.024.
[50] A. Okuniewski, D. Rosiak, J. Chojnacki, B. Becker, Coordination polymers and molecular structures among complexes of mercury(II) halides with selected 1-benzoylthioureas, Polyhedron 90 (2015) 47–57, https://doi.org/10.1016/j.poly.2015.01.035.
[51] L.H. Doerrer, Metallophilic interactions in double salts: toward 1d metal atom chains, Comments Mod. Chem. 29 (2008) 93–127, https://doi.org/10.1080/02603590802310760.
[52] L.H. Doerrer, Steric and electronic effects in metallophilic double salts, Dalton Trans. 39 (2010) 3543–3553, https://doi.org/10.1039/B920389C.
[53] M.A. Spackman, D. Jayatilaka, Hirshfeld surface analysis, CrystEngComm 11 (2009) 19–32, https://doi.org/10.1039/B818330A.
[54] M.A. Spackman, J.J. McKinnon, Fingerprinting intermolecular interactions in molecular crystals, CrystEngComm 4 (2002) 378–392, https://doi.org/

10.1039/B203191B.
[55] S.K. Wolff, D.J. Grimwood, J.J. McKinnon, M.J. Turner, D. Jayatilaka, M.A. Spackman, Crystal Explorer, University of Western Australia, 2012.
[56] A. Bondi, van der Waals volumes and radii, J. Phys. Chem. 68 (1964) 441–451, https://doi.org/10.1021/j100785a001.
[57] M.C. Gimeno, J.M. López-de-Luzuriaga, E. Manso, M. Monge, M.E. Olmos, M. Rodríguez-Castillo, M.-T. Tena, D.P. Day, E.J. Lawrence, G.G. Wildgoose, Synthesis, photochemical, and redox properties of gold(I) and gold(III) pincer complexes incorporating a 2,2′:6′,2″-terpyridine ligand framework, Inorg. Chem. 54 (2015) 10667–10677, https://doi.org/10.1021/acs.inorgchem.5b01477.
[58] K. Czerwińska, M. Golec, M. Skonieczna, J. Palion-Gazda, D. Zygadło, A. Szlapa-Kula, S. Krompiec, B. Machura, A. Szurko, Cytotoxic gold(III) complexes incorporating a 2,2′:6′,2″-terpyridine ligand framework – the impact of the substituent in the 4′-position of a terpy ring, Dalton Trans. 46 (2017) 3381–3392, https://doi.org/10.1039/C6DT04584G.
[59] V. Gomez, M.C. Hardwick, C. Hahn, Crystal structure analysis of two chloro(2,2′:6′,2″-terpyridine)gold(III) complexes, J. Chem. Crystallogr. 42 (2012) 824–831, https://doi.org/10.1007/s10870-012-0320-y.
[60] A. Casini, M.C. Diawara, R. Scopelliti, S.M. Zakeeruddin, M. Grätzel, P.J. Dyson, Synthesis, characterisation and biological properties of gold(III) compounds with modified bipyridine and bipyridylamine ligands, Dalton Trans. 39 (2010) 2239–2245, https://doi.org/10.1039/B921019A.
[61] L. Cao, M.C. Jennings, R.J. Puddephatt, Amine–Amide equilibrium in gold(III) complexes and a gold(III)–Gold(I) aurophilic bond, Inorg. Chem. 46 (2007) 1361–1368, https://doi.org/10.1021/ic061911y.
[62] M.A. Cinellu, L. Maiore, G. Minghetti, F. Cocco, S. Stoccoro, A. Zucca, M. Manassero, C. Manassero, Gold(III) adducts with chiral pyridinyl-oxazolines. Synthesis, reactivity of the coordinated ligands, and structural characterizations, Organometallics 28 (2009) 7015–7024, https://doi.org/10.1021/om900841b.
[63] E.M.A. Ratilla, H.M. Brothers, N.M. Kostic, A transition-metal chromophore as a new, sensitive spectroscopic tag for proteins. Selective covalent labeling of histidine residues in cytochromes c with chloro(2,2':6'2"-terpyridine)platinum(II) chloride, J. Am. Chem. Soc. 109 (1987) 4592–4599, https://doi.org/10.1021/ja00249a023.
[64] J.F. Michalec, S.A. Bejune, D.G. Cuttell, G.C. Summerton, J.A. Gertenbach, J.S. Field, R.J. Haines, D.R. McMillin, Long-lived emissions from 4'-substituted Pt(trpy)Cl+ complexes bearing aryl groups. Influence of orbital parentage, Inorg. Chem. 40 (2001) 2193–2200, https://doi.org/10.1021/ic0013126.
[65] D.R. McMillin, J.J. Moore, Luminescence that lasts from Pt(trpy)Cl+ derivatives (trpy=2,2′;6′,2″-terpyridine), Coord. Chem. Rev. 229 (2002) 113–121, https://doi.org/10.1016/S0010-8545(02)00041-3.
[66] D.K. Crites, C.T. Cunningham, D.R. McMillin, Remarkable substituent effects on the photophysics of Pt(4′-X-trpy)Cl+ systems (trpy = 2,2′; 6′,2″-terpyridine), Inorg. Chim. Acta. 273 (1998) 346–353, https://doi.org/10.1016/S0020-1693(97)06082-9.
[67] H.-K. Yip, L.-K. Cheng, K.-K. Cheung, C.-M. Che, Luminescent platinum(II) complexes. Electronic spectroscopy of platinum(II) complexes of 2,2′:6′,2″-terpyridine (terpy) and p-substituted phenylterpyridines and crystal structure of [Pt(terpy)Cl][CF3SO3], J. Chem. Soc., Dalton Trans. (1993) 2933–2938, https://doi.org/10.1039/DT9930002933, 0.
[68] J.F. Michalec, S.A. Bejune, D.R. McMillin, Multiple ligand-based emissions from a platinum(II) terpyridine complex attached to pyrene, Inorg. Chem. 39 (2000) 2708–2709, https://doi.org/10.1021/ic000304m.
[69] M.A. Mansour, R.J. Lachicotte, H.J. Gysling, R. Eisenberg, Syntheses, molecular structures, and spectroscopy of gold(III) dithiolate complexes, Inorg. Chem. 37 (1998) 4625–4632, https://doi.org/10.1021/ic980032b.
[70] S.-W. Lai, M.C.W. Chan, K.-K. Cheung, C.-M. Che, Spectroscopic properties of luminescent platinum(II) complexes containing 4,4‘,4‘‘-Tri-tert-butyl-2,2‘:6‘,2‘‘-terpyridine (tBu3tpy). Crystal structures of [Pt(tBu3tpy)Cl]ClO4 and [Pt(tBu3tpy){CH2C(O)me}]ClO4, Inorg. Chem. 38 (1999) 4262–4267, https://doi.org/10.1021/ic990446k.
[71] M. Monim-ul-Mehboob, M. Altaf, M. Fettouhi, A.A. Isab, M.I.M. Wazeer, M.N. Shaikh, S. Altuwaijri, Synthesis, spectroscopic characterization and anti-cancer properties of new gold(III)–alkanediamine complexes against gastric, prostate and ovarian cancer cells; crystal structure of [Au2(pn)2(Cl)2]Cl2·H2O, Polyhedron 61 (2013) 225–234, https://doi.org/10.1016/j.poly.2013.05.054.
[72] F. Abbate, P. Orioli, B. Bruni, G. Marcon, L. Messori, Crystal structure and solution chemistry of the cytotoxic complex 1,2-dichloro(o-phenanthroline) gold(III) chloride, Inorg. Chim. Acta. 311 (2000) 1–5, https://doi.org/10.1016/S0020-1693(00)00299-1.
[73] G. Marcon, S. Carotti, M. Coronnello, L. Messori, E. Mini, P. Orioli, T. Mazzei, M.A. Cinellu, G. Minghetti, Gold(III) complexes with bipyridyl Ligands: solution chemistry, cytotoxicity, and DNA binding properties, J. Med. Chem. 45 (2002) 1672–1677, https://doi.org/10.1021/jm010997w.
[74] G. Wilkinson, R.D. Gillard, Comprehensive Coordination Chemistry the Synthesis, Reactions, Properties and Applications of Coordination Compounds V3 Main Group and Early Transition Elements, Pergamon Press, United Kingdom, 1987, p. 19039703. http://inis.iaea.org/search/search.aspx?orig_q=RN.
[75] İ. Uçar, A. Bulut, O. Büyükgüngör, Synthesis, crystal structure, EPR and electrochemical studies of copper(II) dipicolinate complex with 2,2′-dipyridylamine ligand, J. Phys. Chem. Solid. 68 (2007) 2271–2277, https://doi.org/10.1016/j.jpcs.2007.06.017.
[76] B.J. Hathaway, D.E. Billing, The electronic properties and stereochemistry of mono-nuclear complexes of the copper(II) ion, Coord. Chem. Rev. 5 (1970) 143–207, https://doi.org/10.1016/S0010-8545(00)80135-6.
[77] M. Casamento, G.E. Arena, C. Lo Passo, I. Pernice, A. Romeo, L.M. Scolaro, Interaction of organometallic cationic complex ions containing terpyridine ligands with nucleic acids: an investigation on aggregative phenomena, Inorg. Chim. Acta. 275–276 (1998) 242–249, https://doi.org/10.1016/S0020-1693(97)06181-1.
[78] H.L.-K. Fu, C. Po, H. He, S.Y.-L. Leung, K.S. Wong, V.W.-W. Yam, Tuning of supramolecular architectures of l-valine-containing dicyanoplatinum(II) 2,2′-bipyridine complexes by metal–metal, π–π stacking, and hydrogen-bonding interactions, Chem. Eur J. 22 (2016) 11826–11836, https://doi.org/10.1002/chem.201601983.
[79] H.-K. Cheng, M.C.-L. Yeung, V.W.-W. Yam, Molecular engineering of platinum(II) terpyridine complexes with tetraphenylethylene-modified alkynyl ligands: supramolecular assembly via Pt···Pt and/or π–π stacking interactions and the formation of various superstructures, ACS Appl. Mater. Interfaces 9 (2017) 36220–36228, https://doi.org/10.1021/acsami.7b11807.
[80] V.C.-H. Wong, C. Po, S.Y.-L. Leung, A.K.-W. Chan, S. Yang, B. Zhu, X. Cui, V.W.-W. Yam, formation of 1D infinite chains directed by metal–metal and/or π–π stacking interactions of water-soluble platinum(II) 2,6-Bis(benzimidazol-2′-yl)pyridine double complex salts, J. Am. Chem. Soc. 140 (2018) 657–666, https://doi.org/10.1021/jacs.7b09770.
[81] S. Altmann, K. Choroba, M. Skonieczna, D. Zygadło, M. Raczyńska-Szajgin, A. Maroń, J.G. Małecki, A. Szłapa-Kula, M. Tomczyk, A. Ratuszna, B. Machura, A. Szurko, Platinum(II) coordination compounds with 4′-pyridyl functionalized 2,2′:6′,2″-terpyridines as an alternative to enhanced chemotherapy efficacy and reduced side-effects, J. Inorg. Biochem. 201 (2019) 110809, https://doi.org/10.1016/j.jinorgbio.2019.110809.
[82] C. Martín-Santos, E. Michelucci, T. Marzo, L. Messori, P. Szumlas, P.J. Bednarski, R. Mas-Ballesté, C. Navarro-Ranninger, S. Cabrera, J. Alemán, Gold(III) complexes with hydroxyquinoline, aminoquinoline and quinoline ligands: synthesis, cytotoxicity, DNA and protein binding studies, J. Inorg. Biochem. 153 (2015) 339–345, https://doi.org/10.1016/j.jinorgbio.2015.09.012.
[83] L. Ronconi, C. Marzano, P. Zanello, M. Corsini, G. Miolo, C. Maccà, A. Trevisan, D. Fregona, Gold(III) dithiocarbamate derivatives for the treatment of Cancer: solution chemistry, DNA binding, and hemolytic properties, J. Med. Chem. 49 (2006) 1648–1657, https://doi.org/10.1021/jm0509288.
[84] A.N. Wein, A.T. Stockhausen, K.I. Hardcastle, M.R. Saadein, S.(Bruce, Peng, D. Wang, D.M. Shin, Z.(Georgia, Chen, J.F. Eichler, Tumor cytotoxicity of 5,6-dimethyl-1,10-phenanthroline and its corresponding gold(III) complex, J. Inorg. Biochem. 105 (2011) 663–668, https://doi.org/10.1016/j.jinorgbio.2011.01.006.
[85] P.M. Olsen, C. Ruiz, D. Lussier, B.K. Le, N. Angel, M. Smith, C.(Brian, Hwang, R. Khatib, J. Jenkins, K. Adams, J. Getcher, F. Tham, Z. (Georgia) Chen, E.H. Wilson, J.F. Eichler, Synthesis, characterization, and antitumor activity of unusual pseudo five coordinate gold(III) complexes: distinct cytotoxic mechanism or expensive ligand delivery systems? J. Inorg. Biochem. 141 (2014) 121–131, https://doi.org/10.1016/j.jinorgbio.2014.08.014.
[86] A.M. Mansour, O.R. Shehab, Lysozyme and DNA binding affinity of Pd(ii) and Pt(ii) complexes bearing charged N , N -pyridylbenzimidazole bidentate ligands, Dalton Trans. 47 (2018) 3459–3468, https://doi.org/10.1039/C7DT04347C.
[87] M. Sirajuddin, S. Ali, A. Badshah, Drug–DNA interactions and their study by UV–Visible, fluorescence spectroscopies and cyclic voltametry, J. Photochem. Photobiol. B Biol. 124 (2013) 1–19, https://doi.org/10.1016/j.jphotobiol.2013.03.013.
[88] Z. Mandegani, Z. Asadi, M. Asadi, H. Reza Karbalaei-Heidari, B. Rastegari, Synthesis, characterization, DNA binding, cleavage activity, cytotoxicity and molecular docking of new nano water-soluble [M(5-CH 2 PPh 3 -3,4-salpyr)](ClO 4) 2 (M = Ni, Zn) complexes, Dalton Trans. 45 (2016) 6592–6611, https://doi.org/10.1039/C5DT04788A.
[89] M. Dostani, A.H. Kianfar, W.A.K. Mahmood, M. Dinari, H. Farrokhpour, M.R. Sabzalian, F. Abyar, M.H. Azarian, An experimental and theoretical study on the interaction of DNA and BSA with novel Ni2+, Cu2+ and VO2+ complexes derived from vanillin bidentate Schiff base ligand, Spectrochim. Acta Mol. Biomol. Spectrosc. 180 (2017) 144–153, https://doi.org/10.1016/j.saa.2017.02.047.
[90] K.C. Skyrianou, F. Perdih, A.N. Papadopoulos, I. Turel, D.P. Kessissoglou, G. Psomas, Nickel–quinolones interaction: Part 5—biological evaluation of nickel(II) complexes with first-, second- and third-generation quinolones, J. Inorg. Biochem. 105 (2011) 1273–1285, https://doi.org/10.1016/j.jinorgbio.2011.06.005.
[91] C. Protogeraki, E.G. Andreadou, F. Perdih, I. Turel, A.A. Pantazaki, G. Psomas, Cobalt(II) complexes with the antimicrobial drug enrofloxacin: structure, antimicrobial activity, DNA- and albumin-binding, Eur. J. Med. Chem. 86 (2014) 189–201, https://doi.org/10.1016/j.ejmech.2014.08.043.
[92] J.-B. Lepecq, C. Paoletti, A fluorescent complex between ethidium bromide and nucleic acids: physical—Chemical characterization, J. Mol. Biol. 27 (1967) 87–106, https://doi.org/10.1016/0022-2836(67)90353-1.
[93] N.C. Garbett, P.A. Ragazzon, J.B. Chaires, Circular dichroism to determine binding mode and affinity of ligand–DNA interactions, Nat. Protoc. 2 (2007) 3166–3172, https://doi.org/10.1038/nprot.2007.475.

[94] Y.-M. Chang, C.K.-M. Chen, M.-H. Hou, Conformational changes in DNA upon ligand binding monitored by circular dichroism, Int. J. Mol. Sci. 13 (2012) 3394–3413, https://doi.org/10.3390/ijms13033394.
[95] O. Novakova, H. Chen, O. Vrana, A. Rodger, P.J. Sadler, V. Brabec, DNA interactions of monofunctional organometallic ruthenium(II) antitumor complexes in cell-free media, Biochemistry 42 (2003) 11544–11554, https://doi.org/10.1021/bi034933u.
[96] S. Sarkar, K. Bhadra, Binding of alkaloid harmalol to DNA: photophysical and calorimetric approach, J. Photochem. Photobiol. B Biol. 130 (2014) 272–280, https://doi.org/10.1016/j.jphotobiol.2013.11.021.
[97] A. Maroń, K. Czerwińska, B. Machura, L. Raposo, C. Roma-Rodrigues, A.R. Fernandes, J.G. Małecki, A. Szlapa-Kula, S. Kula, S. Krompiec, Spectroscopy, electrochemistry and antiproliferative properties of Au(III), Pt(II) and Cu(II) complexes bearing modified 2,2′:6′,2″-terpyridine ligands, Dalton Trans. 47 (2018) 6444–6463, https://doi.org/10.1039/C8DT00558C.
[98] K. Choroba, B. Machura, S. Kula, L.R. Raposo, A.R. Fernandes, R. Kruszynski, K. Erfurt, L.S. Shul'pina, Y.N. Kozlov, G.B. Shul'pin, Copper(II) complexes with 2,2′:6′,2″-terpyridine, 2,6-di(thiazol-2-yl)pyridine and 2,6-di(pyrazin-2-yl) pyridine substituted with quinolines. Synthesis, structure, antiproliferative activity, and catalytic activity in the oxidation of alkanes and alcohols with peroxides, Dalton Trans. 48 (2019) 12656–12673, https://doi.org/10.1039/C9DT01922G.
[99] S. Fulda, K.-M. Debatin, Extrinsic versus intrinsic apoptosis pathways in anticancer chemotherapy, Oncogene 25 (2006) 4798–4811, https://doi.org/10.1038/sj.onc.1209608.
[100] K. Choroba, L.R. Raposo, J. Palion-Gazda, E. Malicka, K. Erfurt, B. Machura, A.R. Fernandes, In vitro antiproliferative effect of vanadium complexes bearing 8-hydroxyquinoline-based ligands – the substituent effect, Dalton Trans. 49 (2020) 6596–6606, https://doi.org/10.1039/D0DT01017K.
[101] K. Choroba, B. Machura, L.R. Raposo, J.G. Małecki, S. Kula, M. Pająk, K. Erfurt, A.M. Maroń, A.R. Fernandes, Platinum(II) complexes showing high cytotoxicity toward A2780 ovarian carcinoma cells, Dalton Trans. 48 (2019) 13081–13093, https://doi.org/10.1039/C9DT02894C.
[102] K. Malarz, D. Zych, R. Gawecki, M. Kuczak, R. Musioł, A. Mrozek-Wilczkiewicz, New derivatives of 4′-phenyl-2,2':6′,2″-terpyridine as promising anticancer agents, Eur. J. Med. Chem. (2020) 113032, https://doi.org/10.1016/j.ejmech.2020.113032.
[103] X. Gao, X. Li, C.-T. Ho, X. Lin, Y. Zhang, B. Li, Z. Chen, Cocoa tea (Camellia ptilophylla) induces mitochondria-dependent apoptosis in HCT116 cells via ROS generation and PI3K/Akt signaling pathway, Food Res. Int. 129 (2020) 108854, https://doi.org/10.1016/j.foodres.2019.108854.
[104] D. Ribatti, The chick embryo chorioallantoic membrane (CAM) assay, Reprod. Toxicol. 70 (2017) 97–101, https://doi.org/10.1016/j.reprotox.2016.11.004.
[105] I. Zuazo-Gaztelu, O. Casanovas, Unraveling the role of angiogenesis in cancer ecosystems, Front. Oncol. 8 (2018), https://doi.org/10.3389/fonc.2018.00248.
[106] T. Klemens, A. Świtlicka-Olszewska, B. Machura, M. Grucela, E. Schab-Balcerzak, K. Smolarek, S. Mackowski, A. Szlapa, S. Kula, S. Krompiec, P. Lodowski, A. Chrobok, Rhenium(I) terpyridine complexes – synthesis, photophysical properties and application in organic light emitting devices, Dalton Trans. 45 (2016) 1746–1762, https://doi.org/10.1039/C5DT04093K.
[107] A. Maroń, A. Szlapa, T. Klemens, S. Kula, B. Machura, S. Krompiec, J.G. Małecki, A. Świtlicka-Olszewska, K. Erfurt, A. Chrobok, Tuning the photophysical properties of 4′-substituted terpyridines – an experimental and theoretical study, Org. Biomol. Chem. 14 (2016) 3793–3808, https://doi.org/10.1039/C6OB00038J.
[108] A. Maroń, S. Kula, A. Szlapa-Kula, A. Świtlicka, B. Machura, S. Krompiec, J.G. Małecki, R. Kruszyński, A. Chrobok, E. Schab-Balcerzak, S. Kotowicz, M. Siwy, K. Smolarek, S. Maćkowski, H. Janeczek, M. Libera, 2,2′:6′,2″-Terpyridine analogues: structural, electrochemical, and photophysical properties of 2,6-Di(thiazol-2-yl)pyridine derivatives, Eur. J. Org Chem. 2017 (2017) 2730–2745, https://doi.org/10.1002/ejoc.201700141.
[109] P.R.O. CrysAlis, Oxford Diffraction Ltd, Yarnton, England, 2011.
[110] G.M. Sheldrick, A short history of SHELX, Acta Cryst A 64 (2008) 112–122, https://doi.org/10.1107/S0108767307043930.
[111] G.M. Sheldrick, Crystal structure refinement with SHELXL, Acta Cryst C 71 (2015) 3–8, https://doi.org/10.1107/S2053229614024218.
[112] M.E. Reichmann, S.A. Rice, C.A. Thomas, P. Doty, A further examination of the molecular weight and size of desoxypentose nucleic acid, J. Am. Chem. Soc. 76 (1954) 3047–3053, https://doi.org/10.1021/ja01640a067.
[113] J. Marmur, A procedure for the isolation of deoxyribonucleic acid from micro-organisms, J. Mol. Biol. 3 (1961) 208, https://doi.org/10.1016/S0022-2836(61)80047-8. IN1.
[114] R. Hajian, P. Hossaini, Z. Mehrayin, P.M. Woi, N. Shams, DNA-binding studies of valrubicin as a chemotherapy drug using spectroscopy and electrochemical techniques, Journal of Pharmaceutical Analysis 7 (2017) 176–180, https://doi.org/10.1016/j.jpha.2017.01.003.
[115] K. Sakthikumar, R.V. Solomon, J.D. Raja, Spectro-electrochemical assessments of DNA/BSA interactions, cytotoxicity, radical scavenging and pharmacological implications of biosensitive and biologically active morpholine-based metal(II) complexes: a combined experimental and computational investigation, RSC Adv. 9 (2019) 14220–14241, https://doi.org/10.1039/C8RA09218D.
[116] S.N. Mbugua, L.W. Njenga, R.A. Odhiambo, S.O. Wandiga, M. Meyer, N. Sibuyi, R.A. Lalancette, M.O. Onani, Synthesis, characterization, and DNA-binding kinetics of new Pd(II) and Pt(II) thiosemicarbazone complexes: spectral, structural, and anticancer evaluation, J. Chem. 2020 (2020), e3863269, https://doi.org/10.1155/2020/3863269.
[117] L.R. Raposo, A. Silva, D. Silva, C. Roma-Rodrigues, M. Espadinha, P.V. Baptista, M.M.M. Santos, A.R. Fernandes, Exploiting the antiproliferative potential of spiropyrazoline oxindoles in a human ovarian cancer cell line, Bioorg. Med. Chem. 30 (2021) 115880, https://doi.org/10.1016/j.bmc.2020.115880.
[118] O.A. Lenis-Rojas, A.R. Fernandes, C. Roma-Rodrigues, P.V. Baptista, F. Marques, D. Pérez-Fernández, J. Guerra-Varela, L. Sánchez, D. Vázquez-García, M.L. Torres, A. Fernández, J.J. Fernández, Heteroleptic mononuclear compounds of ruthenium(II): synthesis, structural analyses, in vitro antitumor activity and in vivo toxicity on zebrafish embryos, Dalton Trans. 45 (2016) 19127–19140, https://doi.org/10.1039/C6DT03591D.
[119] Z. Ma, B. Zhang, M.F.C.G. da Silva, J. Silva, A.S. Mendo, P.V. Baptista, A.R. Fernandes, A.J.L. Pombeiro, Synthesis, characterization, thermal properties and antiproliferative potential of copper(II) 4′-phenyl-terpyridine compounds, Dalton Trans. 45 (2016) 5339–5355, https://doi.org/10.1039/C5DT02744F.
[120] C. Roma-Rodrigues, G. Malta, D. Peixoto, L.M. Ferreira, P.V. Baptista, A.R. Fernandes, P.S. Branco, Synthesis of new hetero-arylidene-9(10H)-anthrone derivatives and their biological evaluation, Bioorg. Chem. 99 (2020) 103849, https://doi.org/10.1016/j.bioorg.2020.103849.
[121] D. Sequeira, P.V. Baptista, R. Valente, M.F.M. Piedade, M.H. Garcia, T.S. Morais, A.R. Fernandes, Cu(I) complexes as new antiproliferative agents against sensitive and doxorubicin resistant colorectal cancer cells: synthesis, characterization, and mechanisms of action, Dalton Trans. 50 (2021) 1845–1865, https://doi.org/10.1039/D0DT03566A.
[122] C. Roma-Rodrigues, A. Heuer-Jungemann, A.R. Fernandes, A.G. Kanaras, P.V. Baptista, Peptide-coated gold nanoparticles for modulation of angiogenesis in vivo, Int. J. Nanomed. 11 (2016) 2633–2639, https://doi.org/10.2147/IJN.S108661.
[123] C. Roma-Rodrigues, A.R. Fernandes, P.V. Baptista, Counteracting the effect of leukemia exosomes by antiangiogenic gold nanoparticles, Int. J. Nanomed. 14 (2019) 6843–6854, https://doi.org/10.2147/IJN.S215711.